

Self-interacting Dark Matter via Right Handed Neutrino Portal

Debasish Borah,^{1,*} Manoranjan Dutta,^{2,†} Satyabrata Mahapatra,^{2,‡} and Narendra Sahu^{2,§}

¹*Department of Physics, Indian Institute of Technology Guwahati, Assam 781039, India*

²*Department of Physics, Indian Institute of Technology Hyderabad,
Kandi, Sangareddy 502284, Telangana, India*

Abstract

We propose a self-interacting dark matter (DM) scenario with right handed neutrino (RHN) portal to the standard model (SM). The dark sector consists of a particle DM, assumed to be a Dirac fermion, and a light mediator in terms of a dark Abelian vector boson to give rise to the required velocity dependent self-interactions in agreement with astrophysical observations. Irrespective of thermal or non-thermal production of such a DM, its final relic remains under-abundant due to efficient annihilation rates of DM into light mediators by virtue of large self-interaction coupling. We then show that a feeble portal of DM-SM interaction via RHN offers a possibility to fill the relic deficit of DM via the late decay of RHN. As RHN also arises naturally in seesaw models explaining the origin of light neutrino masses, we outline two UV complete realizations of the minimal setup in terms of scotogenic and gauged $B - L$ frameworks where connection to neutrino mass and other phenomenology like complementary discovery prospects are discussed.

*Electronic address: dborah@iitg.ac.in

†Electronic address: ph18resch11007@iith.ac.in

‡Electronic address: ph18resch11001@iith.ac.in

§Electronic address: nsahu@phy.iith.ac.in

I. INTRODUCTION

Presence of dark matter (DM), a non-luminous, non-baryonic form of matter in the present universe in large proportions is supported by irrefutable evidences gathered at several astrophysics and cosmology based experiments over last few decades. While astrophysical experiments reveal the presence of DM locally at different scales like galaxy, clusters [1–3], cosmological experiments like Planck, WMAP predict around 26.8% of the present universe to be made up of DM [4, 5]. In terms of density parameter Ω_{DM} and $h = \text{Hubble Parameter}/(100 \text{ km s}^{-1}\text{Mpc}^{-1})$, the present abundance of this form of matter, popularly known as dark matter (DM), is conventionally reported as [5]

$$\Omega_{\text{DM}}h^2 = 0.120 \pm 0.001 \tag{1}$$

at 68% CL. While astrophysical evidences are based on low redshift measurements, cosmological measurements rely upon the benchmark Λ CDM model in order to extrapolate their findings at the scale of recombination to the present epoch. In the standard model of cosmology or Λ CDM model, CDM refers to cold dark matter (indicating collision-less nature of DM) while Λ refers to the cosmological constant proposed to be responsible for late acceleration of the universe. Given that DM has a particle origin like visible matter, it is known that none of the Standard Model (SM) particles can satisfy all the criteria of a particle DM candidate. While several beyond standard model (BSM) proposals exist in the literature for DM, none of them have shown up in experiments yet. Perhaps the most popular DM framework is the weakly interacting massive particle (WIMP) paradigm where a DM particle having mass and interactions similar to those around the electroweak scale gives rise to the observed relic after thermal freeze-out, a remarkable coincidence often referred to as the *WIMP Miracle* [6].

Although the standard model of cosmology or Λ CDM remains in good agreement with large scale structure of the universe, it suffers from several small scale issues like too-big-to-fail, missing satellite and core-cusp problems [7, 8]. One appealing solution to such small scale problems of CDM, proposed by Spergel and Steinhardt [9] is known as the self-interacting dark matter (SIDM) paradigm. Earlier studies can be found in [10, 11]. The advantage of SIDM, as opposed to collision-less CDM, is the way it solves the above-mentioned problems at small scales while reproducing the standard CDM halos at large radii to be in agreement with observations. This is possible as the self-interacting scattering rate

is proportional to DM density. The required self-interaction is often quantified in terms of cross section to DM mass as $\sigma/m \sim 1 \text{ cm}^2/\text{g} \approx 2 \times 10^{-24} \text{ cm}^2/\text{GeV}$ [12–17]. Such large self-interacting cross sections of DM can be naturally realized in scenarios where DM has a light mediator. In such a scenario, self-interaction is stronger for smaller DM velocities such that it can have large impact on small scale structure. On the other hand, the velocity dependent self-interaction gets reduced at larger scales (due to large velocities of DM) to be remain consistent with large scale CDM predictions [12–15, 18–21]. While both scalar or vector boson can act like mediators of DM self-interactions, it is more natural to vector mediators as they can be realized within gauge extensions of the SM. For example, Abelian gauge extended model with a vector like fermion DM charged under this symmetry can give rise to simple SIDM scenarios where the same gauge symmetry can also lead to DM stability. Such a dark sector comprising of DM and light mediator can not be completely hidden and there should be some coupling of the mediator with the SM particles which can bring DM and SM sectors to equilibrium in the early universe or lead to the production of DM from the SM bath. The same DM-SM coupling can also be probed at DM direct detection experiments as well [22, 23]. Several model building efforts have been made to realize such scenarios. For example, see [24–31] and references therein.

We consider a vector like fermion singlet charged under a $U(1)_D$ gauge symmetry as DM. The singlet fermion DM has light mediator interactions in terms of $U(1)_D$ gauge boson Z' having mass which is a few order of magnitudes lighter than DM mass, required for desired SIDM phenomenology. Since the required self-interaction constrains the corresponding gauge coupling to be sizeable, DM relic usually gets under-abundant due to large annihilation rate of DM into Z' pairs. We consider a tiny kinetic mixing between $U(1)_D$ and $U(1)_Y$ of the SM by virtue of which DM can be produced from the SM bath via freeze-in mechanism [32, 33]. However, due to strong annihilation rate of DM into Z' pairs, the final relic remains under-abundant. This requires some additional source of DM production to fill the deficit caused due to strong DM annihilations into Z' pairs.

In addition to DM, the SM also can not explain the origin of neutrino mass and mixing, as verified at neutrino oscillation experiments [4, 34]. BSM framework must be invoked to explain non-zero neutrino mass as in the SM, there is no way to couple the left handed neutrinos to the Higgs field in the renormalisable Lagrangian due to the absence of right handed neutrinos. Conventional neutrino mass models based on seesaw mechanism [35–43]

typically involve introduction of heavy fields like right handed neutrinos (RHN).

Motivated by these, we consider a self-interacting dark matter scenario where one of the RHNs, introduced for the purpose of generating light neutrino masses, can also play a non-trivial role in late time non-thermal production of DM, thus filling the deficit caused due to strong DM annihilations into Z' . This gives rise to RHN portal SIDM scenario while the RHN is connected to light neutrino masses. It should also be noted that neutrino portal DM have been studied in different contexts in earlier works like [44–56]. However, in most of these works, either DM coupling directly with the SM lepton doublet was considered or a portal via heavy right handed or Dirac neutrinos responsible for DM freeze-out or freeze-in were discussed. In [56], DM-SM coupling via RHN was considered where RHNs are part of light Dirac neutrino with interesting cosmological consequences due to enhanced relativistic degrees of freedom ΔN_{eff} . In the present work, the RHNs can be produced thermally from SM bath with the lightest of them acquiring a thermal relic after freeze-out which then gets converted into SIDM relic due to its late time decay into the latter. After showing the generic features of this setup relevant for the required self-interactions and relic abundance of DM, we consider two specific seesaw models namely, gauged $B - L$ and scotogenic models both of which can lead to thermal production of the RHN and generate its required relic. We then constrain the model parameters from the requirement of generating correct relic abundance of the lightest RHN which gets converted into SIDM relic later. We also find that the models remain predictive at experiments like the large hadron collider (LHC) and experiments looking for charged lepton flavour violation, in addition to experiments related to astrophysical observations as well as DM direct detection.

This paper is organized as follows. In section II, we present the minimal setup of RHN portal SIDM showing the details of self-interaction, relic abundance and direct detection prospects. In section III, we outline two specific UV complete realizations discussing the connection to neutrino mass and other phenomenological prospects. We finally conclude in section IV.

II. SIDM VIA RHN PORTAL

In this section, we discuss the basic ingredients of the model and relevant phenomenology. The BSM particle content is shown in table I along with their transformations under the

gauge symmetry. The SM gauge symmetry is extended by an Abelian $U(1)_D$ gauge symmetry under which an SM singlet Dirac fermion χ is charged. The right handed neutrino N_R uncharged under $U(1)_D$ can act like a portal between the SM and dark sectors. A singlet scalar Φ with non-zero $U(1)_D$ charge not only lead to spontaneous breaking of $U(1)_D$, but also couples N_R with DM fermion χ which plays a crucial role in generating observed DM relic.

Fields		$SU(3)_C \otimes SU(2)_L \otimes U(1)_Y \otimes U(1)_D$			
Fermion	N_R	1	1	0	0
	χ	1	1	0	1
Scalars	Φ	1	1	0	-1

TABLE I: Charge assignment of BSM fields under the gauge group $G \equiv G_{\text{SM}} \otimes U(1)_D$ where $G_{\text{SM}} \equiv SU(3)_c \otimes SU(2)_L \otimes U(1)_Y$.

Owing to the BSM particle content and their charge assignments as shown in table I, the generic Lagrangian with the interactions relevant for determining the DM abundance in the considered scenario is given by

$$\mathcal{L}_{DM} \supset i \bar{\chi} \gamma^\mu D_\mu \chi - m_\chi \bar{\chi} \chi - \frac{1}{2} M_{N_R} \bar{N}_R^c N_R - y \chi \Phi N_R - y' \bar{\chi} \Phi^* N_R + \frac{\epsilon}{2} B^{\alpha\beta} Y_{\alpha\beta} \quad (2)$$

where $D_\mu = \partial_\mu + ig_D Z'_\mu$ and $B^{\alpha\beta}, Y_{\alpha\beta}$ are the field strength tensors of $U(1)_D, U(1)_Y$ respectively with ϵ being the kinetic mixing between them. We consider the two Yukawa couplings between χ, N_R to be identical ($y = y'$) for simplicity and denote them by y hereafter. The Lagrangian involving singlet scalar Φ can be written as

$$\mathcal{L}_\Phi = (D_\mu \Phi)^\dagger (D^\mu \Phi) + m_\Phi^2 \Phi^\dagger \Phi - \lambda_\phi (\Phi^\dagger \Phi)^2 - \lambda_{\Phi H} (\Phi^\dagger \Phi) (H^\dagger H) \quad (3)$$

The singlet scalar can acquire a non-zero vacuum expectation value (VEV) $\langle \Phi \rangle = u$ giving rise to $U(1)_D$ gauge boson mass $M_{Z'} = g_D u$. The same singlet scalar VEV can also generate a mixing between χ and N_R leading to pseudo-Dirac states. However, the corresponding Yukawa coupling Y is very small as required from relic abundance criteria to be discussed below. Therefore, we continue to consider DM as pure Dirac states assuming $Y u \ll M_{N_R}$. While there can be multiple copies of RHNs, as required from neutrino mass requirement, we consider only the lightest of them (N_1) to couple to DM for the sake of minimality.

A. Dark Matter Self-interaction

As discussed above, the DM is assumed to be a pure Dirac fermion having vector like couplings to Z' of type $g'Z'_\mu\bar{\chi}\gamma^\mu\chi$. As a result the DM can have elastic self-scatterings mediated via Z' . In order to have sufficient self-interactions, one needs to satisfy the requirement on cross-section as $\sigma \sim 1 \text{ cm}^2(\frac{m_\chi}{g}) \approx 2 \times 10^{-24} \text{ cm}^2(\frac{m_\chi}{\text{GeV}})$, which is many orders of magnitude larger than the typical weak-scale cross-section ($\sigma \sim 10^{-36} \text{ cm}^2$). Such large self-interacting cross-sections can naturally be realized with a light mediator or a dark boson much lighter compared to the typical weak scale mediators. For such light mediator which is same as $U(1)_D$ gauge boson Z' in our setup, the self-interaction of non-relativistic DM can be described by a Yukawa type potential given as

$$V(r) = \pm \frac{\alpha_D}{r} e^{-M_{Z'} r}. \quad (4)$$

In the above equation, the + (-) sign denotes repulsive (attractive) potential and $\alpha_D = g_D^2/4\pi$ is the dark fine structure constant. While $\chi\bar{\chi}$ interaction is attractive, $\chi\chi$ and $\bar{\chi}\bar{\chi}$ are repulsive. To capture the relevant physics of forward scattering divergence for the self-interaction we define the transfer cross-section σ_T as [7, 13, 21]

$$\sigma_T = \int d\Omega (1 - \cos\theta) \frac{d\sigma}{d\Omega}. \quad (5)$$

In the Born Limit ($\alpha_D m_\chi/M_{Z'} \ll 1$), for both attractive as well as repulsive potentials, the transfer cross-section is

$$\sigma_T^{\text{Born}} = \frac{8\pi\alpha_D^2}{m_\chi^2 v^4} \left(\ln(1 + m_\chi^2 v^2/M_{Z'}^2) - \frac{m_\chi^2 v^2}{M_{Z'}^2 + m_\chi^2 v^2} \right). \quad (6)$$

Outside the Born regime ($\alpha_D m_\chi/M_{Z'} \geq 1$), we have two distinct regions *viz* the classical region and the resonance region. In the classical limit ($m_\chi v/M_{Z'} \geq 1$), the solutions for an attractive potential is given by [21, 57, 58]

$$\sigma_T^{\text{classical}}(\text{Attractive}) = \begin{cases} \frac{4\pi}{M_{Z'}^2} \beta^2 \ln(1 + \beta^{-1}) & \beta \leq 10^{-1} \\ \frac{8\pi}{M_{Z'}^2} \beta^2 / (1 + 1.5\beta^{1.65}) & 10^{-1} \leq \beta \leq 10^3 \\ \frac{\pi}{M_{Z'}^2} (\ln \beta + 1 - \frac{1}{2} \ln^{-1} \beta) & \beta \geq 10^3 \end{cases} \quad (7)$$

$$\sigma_T^{\text{classical}}(\text{Repulsive}) = \begin{cases} \frac{2\pi}{M_{Z'}^2} \beta^2 \ln(1 + \beta^{-2}) & \beta \leq 1 \\ \frac{\pi}{M_{Z'}^2} (\ln 2\beta^2 - \ln \ln 2\beta)^2 & \beta \geq 1 \end{cases} \quad (8)$$

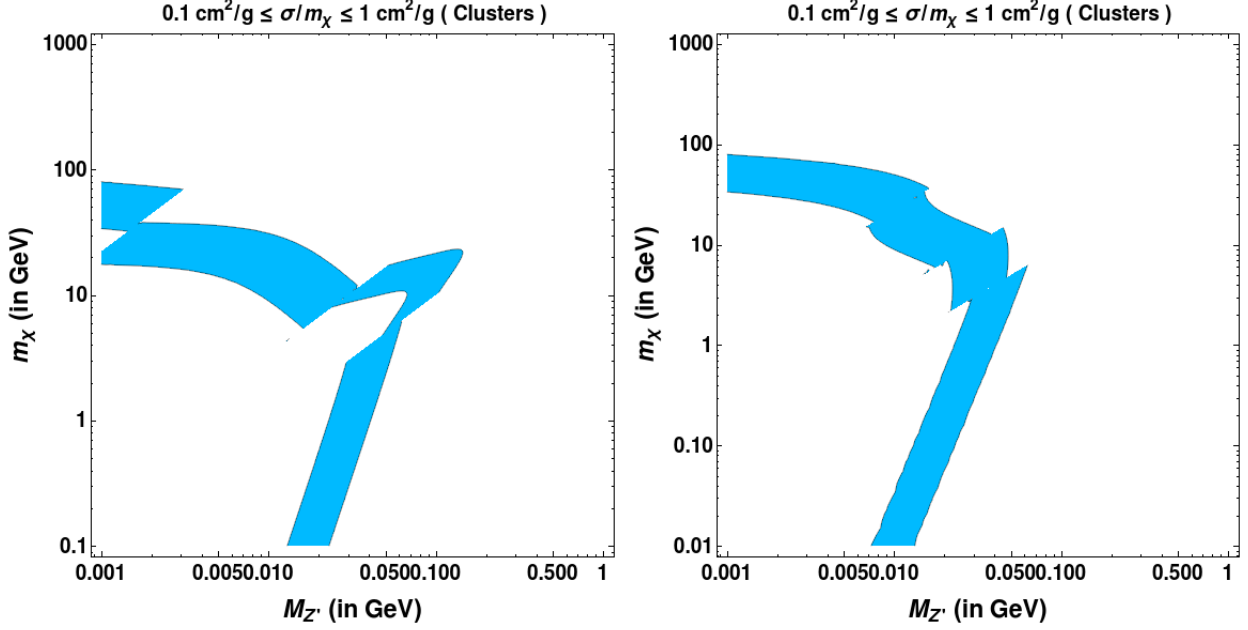


FIG. 1: [Left]: Attractive; [Right]: Repulsive self-interaction cross-section in the range $0.1 - 1 \text{ cm}^2/\text{g}$ for clusters ($v \sim 1000 \text{ km/s}$). Sky blue colour represents regions of parameter space where $0.1 \text{ cm}^2/\text{g} < \sigma/m_\chi < 1 \text{ cm}^2/\text{g}$.

where $\beta = 2\alpha_D M_{Z'}/(m_\chi v^2)$.

Both the Born and the classical regimes do not provide us the mild velocity dependence in the cross-section required to explain the small-scale issues of CDM. However one interesting regime lies outside the classical regime for $\alpha_D m_\chi/M_{Z'} \geq 1, m_\chi v/M_{Z'} \leq 1$. This is the resonant regime, where quantum mechanical resonances and anti-resonances appear in σ_T corresponding to (quasi-)bound states in the potential. In this regime, an analytical formula for σ_T does not exist, and one has to solve the non-relativistic Schrodinger equation by partial wave analysis. Here we use the non-perturbative results for s-wave ($l=0$) scattering within the resonant regime obtained by approximating the Yukawa potential to be a Hulthen potential $\left(V(r) = \pm \frac{\alpha_D \delta e^{-\delta r}}{1 - e^{-\delta r}}\right)$, which is given by [21]

$$\sigma_T^{\text{Hulthen}} = \frac{16\pi \sin^2 \delta_0}{m_\chi^2 v^2} \quad (9)$$

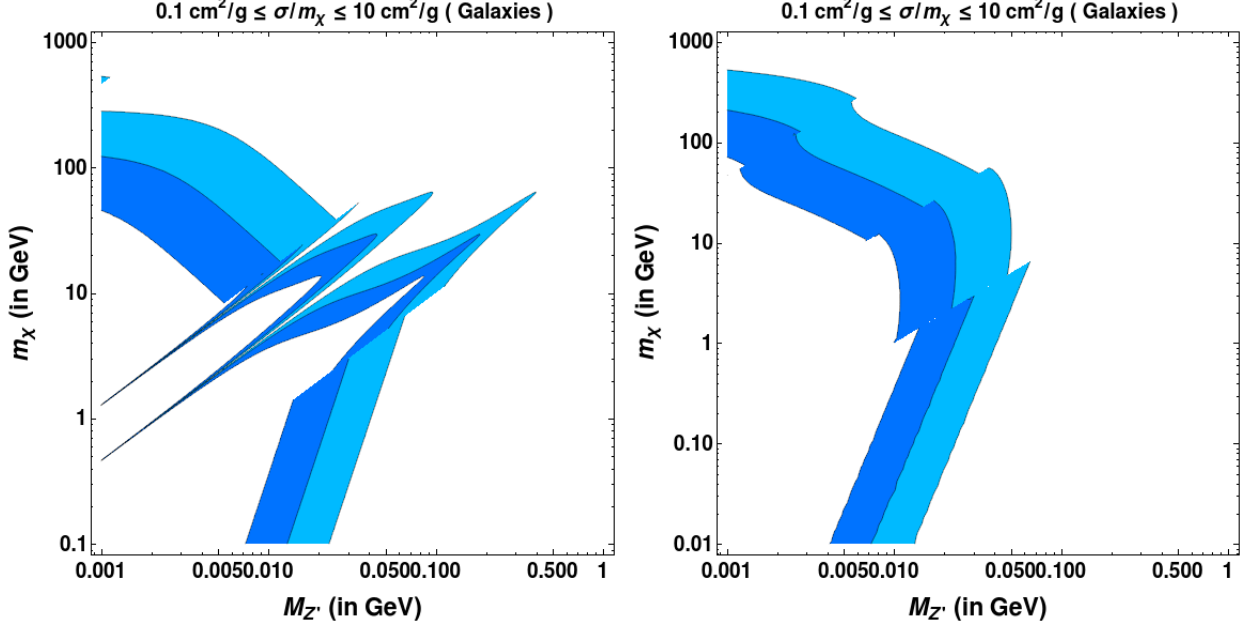


FIG. 2: [Left]: Attractive; [Right]: Repulsive self-interaction cross-section in the range 0.1 – 10 cm^2/g for galaxies ($v \sim 200$ km/s). Blue colour represents regions of parameter space where $1 \text{ cm}^2/\text{g} < \sigma/m_\chi < 10 \text{ cm}^2/\text{g}$; Sky blue colour represents regions of parameter space where $0.1 \text{ cm}^2/\text{g} < \sigma/m_\chi < 1 \text{ cm}^2/\text{g}$.

where $l=0$ phase shift is given in terms of the Γ functions by

$$\delta_0 = \arg\left(\frac{i\Gamma\left(\frac{im_\chi v}{kM_{Z'}}\right)}{\Gamma(\lambda_+)\Gamma(\lambda_-)}\right), \quad \lambda_\pm = \begin{cases} 1 + \frac{im_\chi v}{2kM_{Z'}} \pm \sqrt{\frac{\alpha_D m_\chi}{kM_{Z'}} - \frac{m_\chi^2 v^2}{4k^2 M_{Z'}^2}} & \text{Attractive} \\ 1 + \frac{im_\chi v}{2kM_{Z'}} \pm i\sqrt{\frac{\alpha_D m_\chi}{kM_{Z'}} + \frac{m_\chi^2 v^2}{4k^2 M_{Z'}^2}} & \text{Repulsive} \end{cases} \quad (10)$$

with $k \approx 1.6$ being a dimensionless number.

We use these expressions for DM self-interaction cross-sections considering the astrophysical bounds on required self-interactions namely, σ/m_χ at different scales to constrain the model parameters. Keeping the dark gauge coupling fixed as $g_D = 0.1$, in Fig. 1,2,3, we show the allowed parameter space in m_χ versus $M_{Z'}$ plane which gives rise to the required DM self-interaction cross-section (σ/m_χ) in the range 0.1 – 1 cm^2/g for clusters ($v \sim 1000$ km/s), $\sigma \in 0.1 - 10 \text{ cm}^2/\text{g}$ for galaxies ($v \sim 200$ km/s) and $\sigma \in 0.1 - 100 \text{ cm}^2/\text{g}$ for dwarf galaxies ($v \sim 10$ km/s) respectively. Since the mediator is a vector boson, there exists both attractive and repulsive self-interactions as opposed to the case with scalar mediator giving only attractive self-interactions. The sharp spikes seen in the left panel plots of Fig. 2,3 denote the patterns of quantum mechanical resonances and anti-resonances for the attractive po-

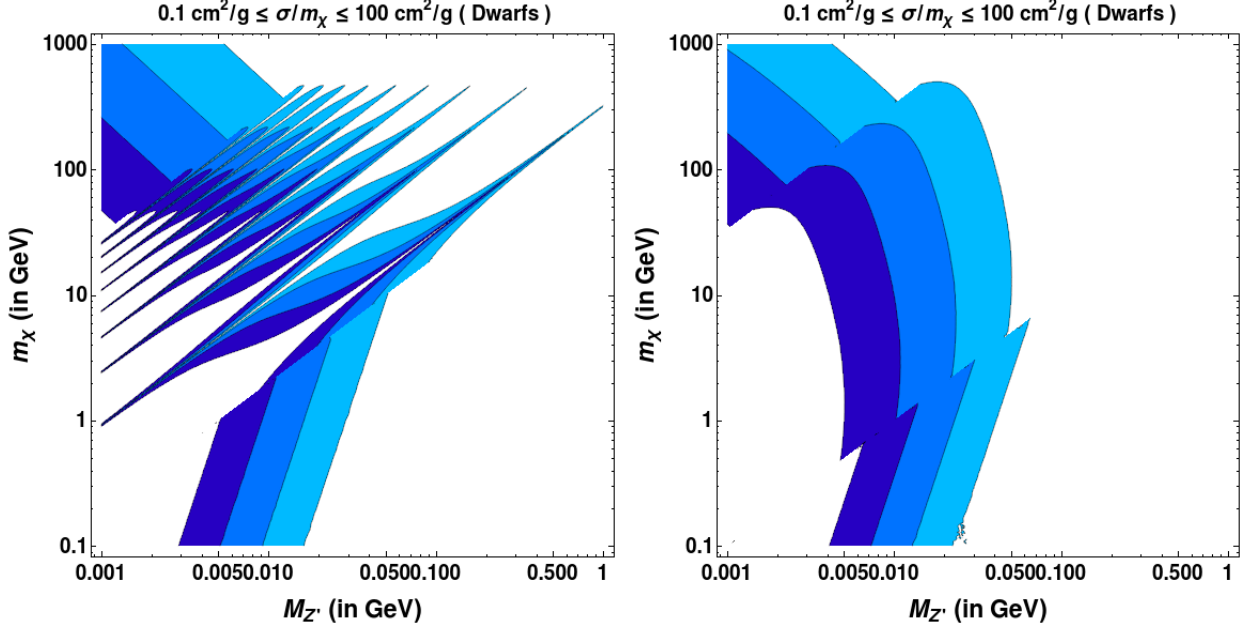


FIG. 3: [Left]: Attractive; [Right]: Repulsive self-interaction cross-section $0.1 - 100 \text{ cm}^2/\text{g}$ for dwarfs ($v \sim 10 \text{ km/s}$). Dark blue colour represents regions of parameter space where $10 \text{ cm}^2/\text{g} < \sigma/m_\chi < 100 \text{ cm}^2/\text{g}$; Blue colour represents regions of parameter space where $1 \text{ cm}^2/\text{g} < \sigma/m_\chi < 10 \text{ cm}^2/\text{g}$; Sky blue colour represents regions of parameter space where $0.1 \text{ cm}^2/\text{g} < \sigma/m_\chi < 1 \text{ cm}^2/\text{g}$.

tential. For a repulsive potential case, such resonances are absent as shown on the right panels of Fig. 2,3. The resonant regime covers a large portion of the parameter space in the m_χ versus $M_{Z'}$ plane. For galactic and dwarf galactic scales with relatively small DM velocities, such features are more dominant. This is due to the fact that for a fixed α_D , the condition $m_\chi v/M_{Z'} < 1$ dictates the onset of non-perturbative quantum mechanical effects. One can notice from these figures that even after using the constraints from required self-interactions, a wide range of DM mass remains allowed even though the mediator mass gets constrained within one or two orders of magnitudes except in the resonance regimes. While discussing other relevant DM phenomenology in upcoming sections, we will compare these allowed regions of parameter space from required self-interactions with the ones obtained using other relevant constraints.

Finally, we show the self-interaction cross-section per unit DM mass as a function of average collision velocity in Fig.4. The data points with error bars include observations of dwarfs (cyan), low surface brightness (LSB) galaxies (blue) and clusters (green)[19, 59].

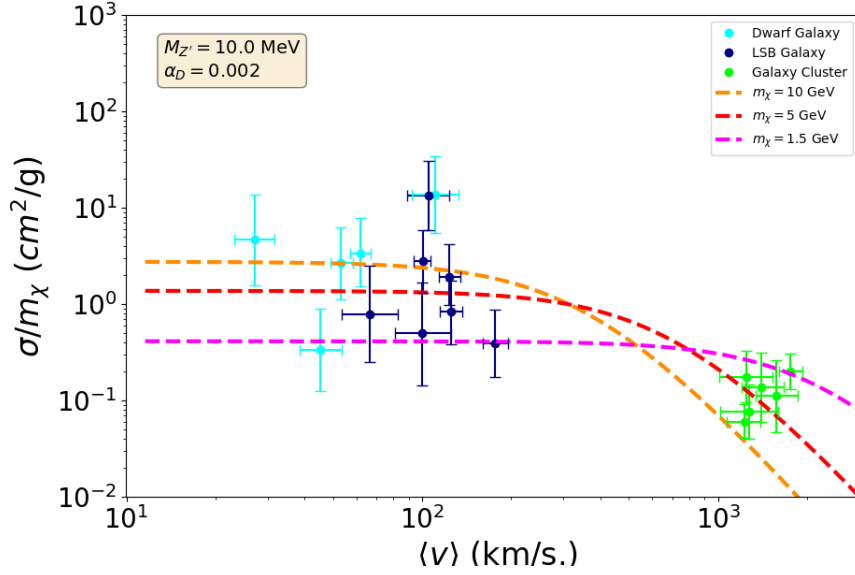


FIG. 4: The self-interaction cross section per unit mass of DM as a function of average collision velocity.

The dashed line correspond to different DM masses while other parameters are fixed as $M_{Z'} = 10$ MeV and $\alpha_D = 0.002$. It is clear from Fig.4 that the SIDM model we adopt can explain astrophysical observations of velocity dependent DM self-interaction appreciably well. It is worth mentioning here that, for fixed DM mass if we increase Z' mass, the DM self-interaction cross-section gradually decreases and may not satisfy the astrophysical observation for the DM mass range we are interested in (*i.e.* 1 – 10 GeV). One can, however, increase the corresponding gauge coupling to compensate for this decrease, as long as we are within perturbative limits.

B. Production of Dark Matter

Several production regimes for self-interacting DM exist in the literature [24–29, 60]. While DM can have large enough self-interaction mediated by the light Z' with sizeable g_D sufficient to address the small-scale issues, it can interact with the thermal bath only via kinetic mixing of neutral vector bosons. Even though DM has coupling with RHN with the latter being assumed to be in thermal bath, the corresponding coupling is required to be small from late freeze-in criteria to be discussed below.

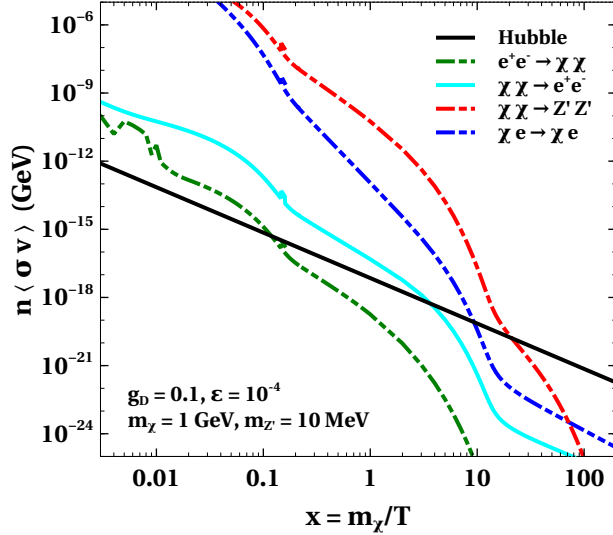


FIG. 5: Comparison of different scattering processes involving DM with Hubble rate of expansion in radiation dominated era for kinetic mixing parameter $\epsilon = 10^{-4}$.

For sizeable kinetic mixing ($\epsilon \geq 10^{-5}$), the DM can be in thermal equilibrium with the SM bath in the early universe. In Fig. 5, we show the comparison of the rates of different processes considering $\epsilon = 10^{-4}$ with the Hubble expansion rate of the universe in a radiation dominated era. For numerical analysis, the model has been implemented in standard packages like LanHEP [61] and CalcHEP [62]. As we can see from Fig. 5, all relevant processes are well above the Hubble expansion rate at early epochs keeping DM χ in thermal equilibrium. However, to get velocity dependent self-scattering we are considering heavier DM compared to the mediator *i.e.*, $m_\chi > M_{Z'}$ and therefore, DM has large annihilation cross section to Z' pairs compared to its annihilation rates into SM particles. This can significantly lead to suppressed thermal relic of DM as we discuss below. The dominant number changing processes contributing to its thermal freeze-out are shown in Fig. 6.

While the right panel diagram of Fig. 6 is suppressed by kinetic mixing, the left panel diagram (for sizeable gauge coupling $g_D \sim 0.1$ and GeV scale DM mass) leads to a cross-section which is much larger than the one governing typical WIMP annihilation. The thermally averaged cross-section for this process can be approximately given by

$$\langle \sigma v \rangle \sim \frac{\pi \alpha_D^2}{m_\chi^2} \quad (11)$$

where $\alpha_D = g_D^2/(4\pi)$. As a consequence, the thermal freeze-out abundance is well below the

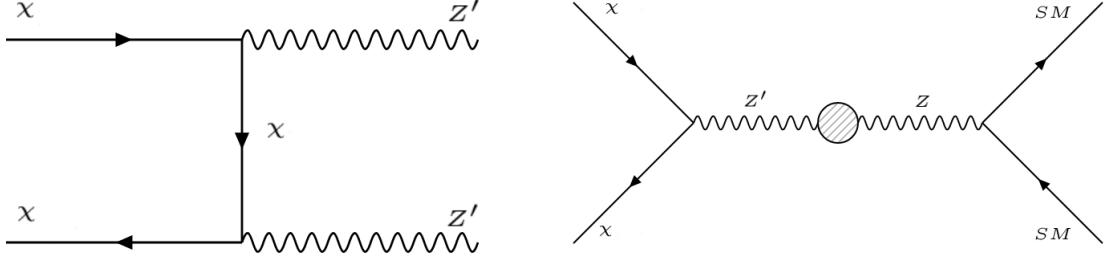


FIG. 6: Feynman diagrams for dominant number changing processes of DM.

correct ballpark given by Eq. (1). This is where the importance of the RHN portal arises as the RHN can decay at late time to DM bringing the relic back to its correct ballpark. To calculate the relic density precisely, we define comoving number densities of these particles as $Y_\chi = n_\chi/s(T)$, $Y_{N_R} = n_{N_R}/s(T)$ with $s(T)$ being the entropy density and write down the coupled Boltzmann equations for the DM χ and the right handed neutrino N_R as follows.

$$\begin{aligned} \frac{dY_{N_R}}{dx} &= -\frac{s(m_\chi)}{x^2 H(m_\chi)} \langle \sigma v \rangle_{\text{F.O.}}^{N_R} (Y_{N_R}^2 - (Y_{N_R}^{\text{eq}})^2) - \frac{x}{H(m_\chi)} \langle \Gamma_{N_R \rightarrow \phi \chi} \rangle Y_{N_R}, \\ \frac{dY_\chi}{dx} &= -\frac{s(m_\chi)}{x^2 H(m_\chi)} \langle \sigma(\chi\chi \rightarrow Z'Z')v \rangle (Y_\chi^2 - (Y_\chi^{\text{eq}})^2) + \frac{x}{H(m_\chi)} \langle \Gamma_{N_R \rightarrow \phi \chi} \rangle Y_{N_R}, \end{aligned} \quad (12)$$

where $x = m_\chi/T$. The evolution of comoving number densities of these particles for a typical set of parameters: ($m_\chi = 1 \text{ GeV}$, $M_{N_R} = 1 \text{ TeV}$, $M_{Z'} = 10 \text{ MeV}$, $g_D = 0.1$) is shown in Fig. 7 by solving the coupled Boltzmann equations given by Eq. (12). While we have not specified the interactions of N_R with SM particles in this minimal setup, we assume N_R to be in equilibrium with the thermal bath initially and thereafter freezes out with freeze-out cross-section $\langle \sigma v \rangle_{\text{F.O.}}^{N_R} = 6 \times 10^{-13} \text{ GeV}^{-2}$. The equilibrium number densities of χ and N_R are shown by dotted green and dotted brown curves respectively in Fig. 7. The thermal freeze-out of the χ is depicted by the dashed blue curve and that of RHN is depicted by the dashed yellow curves. The thermal freeze-out followed by the decay of N_R is depicted by the dashed cyan coloured curve, which lifts the DM relic to the observed value as depicted by the red graph. Similar discussions on DM having deficit in its thermal abundance, followed by late decay of another particle can be found in earlier works [30, 31, 63–67] where a hybrid of freeze-out and freeze-in mechanisms were utilized to get correct DM relic abundance. Use of such hybrid setup in other contexts may be found in [68–70] and references therein.

However it is to be noted such large kinetic mixing can be in tension with DM direct search bounds from CRESST-III [71], XENON1T [72] depending upon DM as well as mediator

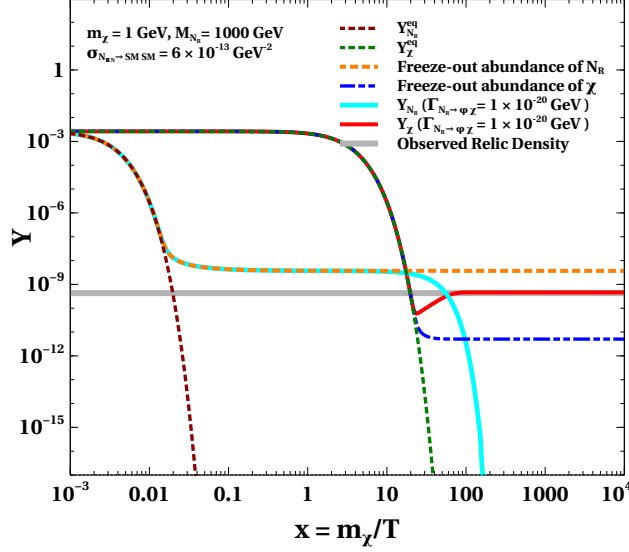


FIG. 7: Comoving number densities of thermal dark sector particles considering different subprocesses indicated in the legends.

masses and gauge coupling. Also, for light Z' in sub-GeV scale, dark photon searches can put such large kinetic mixing in tension with low energy data [73]. To be consistent with such bounds, we consider the kinetic mixing to be very small ($\sim 10^{-8}$), while simultaneously satisfying the large DM self-interaction criteria governed by sizeable g_D and light Z' . But if the kinetic mixing parameter is very small, the DM is not necessarily in thermal equilibrium in the early universe. To check whether DM-SM interactions for such small kinetic mixing can indeed reach equilibrium in the early universe or not, we compare the rates of different annihilation processes with the Hubble expansion rate of the radiation dominated universe. The comparison is shown in Fig. 8 considering kinetic mixing parameter $\epsilon = 10^{-9}$.

From Fig. 8, it is evident that $\chi\chi \rightarrow Z'Z'$ interaction remains in equilibrium until very late epoch $x \sim 10$, while DM-SM number changing interactions mostly remain out of equilibrium throughout. However, the number conserving scattering process DM $e \rightarrow$ DM e , which is responsible for keeping both the sectors in kinetic equilibrium, decouples around $x \sim 0.0007$. So prior to $x \sim 0.0007$, the dark sector temperature (denoted by T') is same as that of thermal bath (denoted by T). After $x \sim 0.0007$, the temperature of the dark sector evolves independently of the thermal bath until $x \sim 100$ when all the dark sector particles including light vector boson Z' become non-relativistic and no longer contribute to the entropy degrees of freedom. Between $x \sim 0.0007$ and $x \sim 100$, the ratio of the visible and dark sector

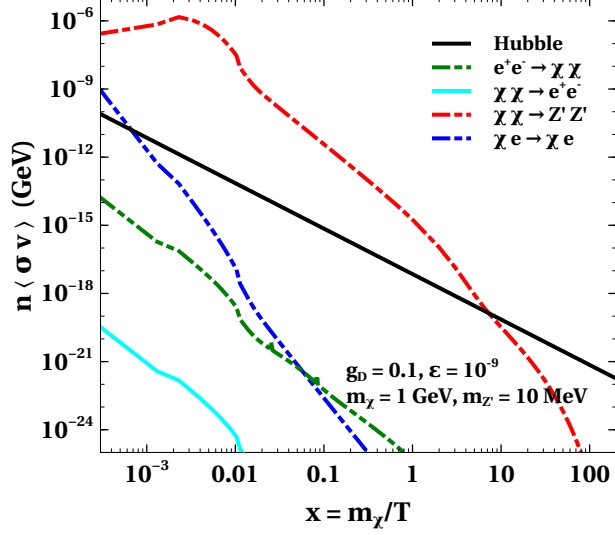


FIG. 8: Comparison of different scattering processes involving DM with Hubble rate of expansion in radiation dominated universe for kinetic mixing parameter $\epsilon = 10^{-9}$.

temperatures can be obtained by conserving the total entropy density separately in the two sectors. Considering the kinetic decoupling temperature to be T_D , we can relate the temperature of the two sectors as :

$$\frac{T'}{T} = \left(\frac{g_{*s}^{\text{SM}}(T)}{g_{*s}^{\text{SM}}(T_D)} \right)^{1/3}. \quad (13)$$

Here $g_{*s}^{\text{SM}}(T)$ is the relativistic entropy degrees of freedom in the SM which goes into the calculation of relativistic entropy density $s(T) = \frac{2\pi^2}{45} g_{*s}(T) T^3$. Since the above relation (13) between two temperatures is valid for $T < T_D$, we naturally have $g_{*s}^{\text{SM}}(T) < g_{*s}^{\text{SM}}(T_D)$ leading to $T' < T$. This is also understood from the fact that SM bath temperature receives additional entropy contributions from the species which keep getting decoupled gradually. Within the decoupled dark sector itself, the DM particles can transfer their entropy into much lighter Z' bosons once T' falls below DM mass. This corresponds to an enhancement of dark sector temperature for $T' < m_{\text{DM}} = m_\chi$ by $(13/6)^{1/3}$, a factor close to unity. We have ignored this additional but tiny enhancement in the numerical calculations to be discussed below. For dark sector temperature, we can similarly define a dimensionless integration variable x' , related to the usual variable x as

$$x' = \frac{m_\chi}{T'} = \left(\frac{T}{T'} \right) x. \quad (14)$$

In the case of small kinetic mixing, we assume negligible initial density for the DM, and the DM can be produced from the bath particles by freeze-in mechanism [32]. However, due to strong $\chi\chi \rightarrow Z'Z'$ cross-section, such non-thermally produced DM will quickly annihilate into light Z' boson pairs depleting the relic further. The right handed neutrino N_R can decay to scalar ϕ and the DM χ at late epoch to bring the relic to the correct ballpark. Unlike the DM whose interactions with the SM bath are suppressed due to tiny kinetic mixing, the right handed neutrino N_R can be in thermal equilibrium with the SM leading to its thermal freeze-out followed by its late decay into DM.

As DM and N_R masses can be very different from each other, the freeze-out abundance of N_R need not necessarily match the required relic density of the DM always. However, both the thermal freeze-out cross-section of N_R ($\langle\sigma v\rangle_{F.O.}^{N_R}$) and the decay width of N_R ($\Gamma_{N_R\rightarrow\phi\chi}$) play crucial roles in determining the the correct relic of the DM. In fact, there exists strong correlation between $\langle\sigma v\rangle_{F.O.}^{N_R}$ and $\Gamma_{N_R\rightarrow\phi\chi}$ from the requirement of producing correct relic of DM of a particular mass, which we discuss below.

To calculate the relic density for freeze-in case with small kinetic mixing, we again define comoving number densities as $Y_\chi = n_\chi/s'(T'(T))$, $Y_{N_R} = n_{N_R}/s(T)$ and write down the coupled Boltzmann equations for DM χ and the right handed neutrino N_R as follows. .

$$\begin{aligned} \frac{dY_{N_R}}{dx} &= -\frac{s(m_\chi)}{x^2 H(m_\chi) \left(\frac{T'}{T}\right)} \langle\sigma v\rangle_{F.O.}^{N_R} (Y_{N_R}^2 - (Y_{N_R}^{eq})^2) - \left(\frac{T'}{T}\right)^2 \frac{x}{H(m_\chi)} \langle\Gamma_{N_R\rightarrow\phi\chi}\rangle Y_{N_R} , \\ \frac{dY_\chi}{dx} &= \left(\frac{T'}{T}\right)^2 \left[\frac{s(m_\chi)}{x^2 H(m_\chi)} \left(\langle\sigma(e^+e^- \rightarrow \chi\chi)v\rangle (Y_\chi^{eq})^2 - \langle\sigma(\chi\chi \rightarrow Z'Z')v\rangle Y_\chi^2 \right) + \frac{x \left(\frac{g_{*s}(T_D)}{g_{*s}(T)}\right)}{H(m_\chi)} \langle\Gamma_{N_R\rightarrow\phi\chi}\rangle Y_{N_R} \right] , \end{aligned} \quad (15)$$

where $x = \frac{m_\chi}{T}$, $s(m_\chi) = \frac{2\pi^2}{45} g_* s m_\chi^3$, $H(m_\chi) = 1.67 g_*^{1/2} \frac{m_\chi^2}{M_{Pl}}$ and $\langle\sigma v\rangle_{F.O.}^{N_R}$ represents the thermally averaged freeze-out cross-section [74] of N_R . Also, $\langle\Gamma_{N_R\rightarrow\phi\chi}\rangle$ represents the thermally averaged decay width of the process $N_R \rightarrow \phi\chi$. The relevant cross-section and decay widths are given in Appendix A. Note that for sufficiently large kinetic mixing, the process $e^+e^- \rightarrow \chi\chi$ becomes both-directional and $T' = T$, *i.e.*, DM comes to thermal equilibrium and we get back to Eq. (12).

To solve the coupled Boltzmann equations given by Eq. (15), we divide the integration range into three regions as follows.

- i) $x < 0.0007$, where both the dark and the visible sectors share the same temperature $T = T'$ (see Fig. 8).

- ii) $0.0007 < x < 100$ where the dark sector is decoupled from the thermal bath and its temperature evolves according to Eq. (13).
- iii) $x > 100$, the dark sector ceases to contribute to relativistic entropy density.

We solve the Boltzmann equations taking into account the temperature evolution in region i) and ii) mentioned above. For calculation of relic density, we consider the freeze-out cross-section of RHN $\langle\sigma v\rangle_{\text{F.O.}}^{N_R}$ and the decay width $\Gamma_{N_R\rightarrow\phi\chi}$ as free parameters and explain the details of how this cross-sections can be realized within the framework of a model in a later section III. We find that there exists interesting correlation between $\langle\sigma v\rangle_{\text{F.O.}}^{N_R}$ and $\Gamma_{N_R\rightarrow\phi\chi}$ to give the correct relic for a DM of particular mass, which also depends upon the mass of N_R . We show the contours of correct relic for different cases in the plane of $\langle\sigma v\rangle_{\text{F.O.}}^{N_R}$ versus $\Gamma_{N_R\rightarrow\phi\chi}$ in the left panel of Fig. 9. We keep Z' mass $M_{Z'}=10$ MeV, with DM and RHN masses as per the following benchmarks.

- i) $m_\chi = 1$ GeV, $M_{N_R} = 1000$ GeV depicted by the thick dashed cyan curve.
- ii) $m_\chi = 1$ GeV, $M_{N_R} = 100$ GeV depicted by the thick dot-dashed green curve.
- iii) $m_\chi = 10$ GeV, $M_{N_R} = 1000$ GeV depicted by the thick dashed blue curve.
- iv) $m_\chi = 10$ GeV, $M_{N_R} = 100$ GeV depicted by the thick dashed red curve.

To analyze the left panel of Fig. 9, let us identify three distinct cases of DM production depending on $\langle\sigma v\rangle_{\text{F.O.}}^{N_R}$ versus $\Gamma_{N_R\rightarrow\phi\chi}$.

Case-I: When $\langle\sigma v\rangle_{\text{F.O.}}^{N_R}$ is very small, the freeze-out abundance of N_R is large and can be comparable to the photon number density. If such a huge abundance is transferred to DM at later epochs, it may lead to overproduction of DM as well. Therefore, to get the correct relic density for the DM, decay of N_R must occur at such an early epoch so that the $\chi\chi \rightarrow Z'Z'$ annihilation is still very active¹. As a result the huge DM relic obtained from N_R decay can still settle down to the observed DM relic due to subsequent annihilation into Z' pairs. For example, the point marked as A ($\langle\sigma v\rangle_{\text{F.O.}}^{N_R} = 1 \times 10^{-20} \text{ GeV}^{-2}$) in the left panel of Fig. 9, indicates a particular value of the N_R freeze-out cross-section with N_R mass 1000 GeV. If the cross-section of N_R is further small, then the freeze-out abundance of N_R can be as large

¹ Note that $\chi\chi \rightarrow Z'Z'$ is active till $x \sim 13$ as seen in Fig. 8.

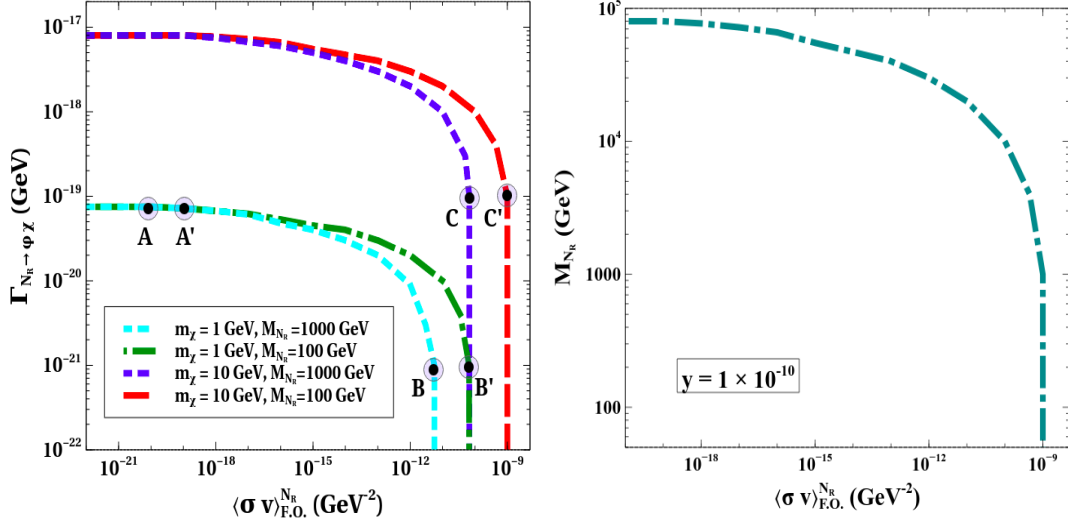


FIG. 9: [Left]: Contours of correct DM relic in the plane of $\langle \sigma v \rangle_{\text{F.O.}}^{N_R}$ versus $\Gamma_{N_R \rightarrow \phi \chi}$. [Right]: Range of RHN mass M_{N_R} for a fixed Yukawa coupling $y = 1 \times 10^{-10}$ giving the decay width in the correct range as shown in the left panel.

as the photon number density. At and below this cross-section, the decay width of N_R to give correct relic density must be $\Gamma_{N_R \rightarrow \phi \chi} = 7.5 \times 10^{-20}$ GeV. For better understanding, we show the corresponding evolution of comoving number densities in the left panel of Fig. 10, to be discussed later.

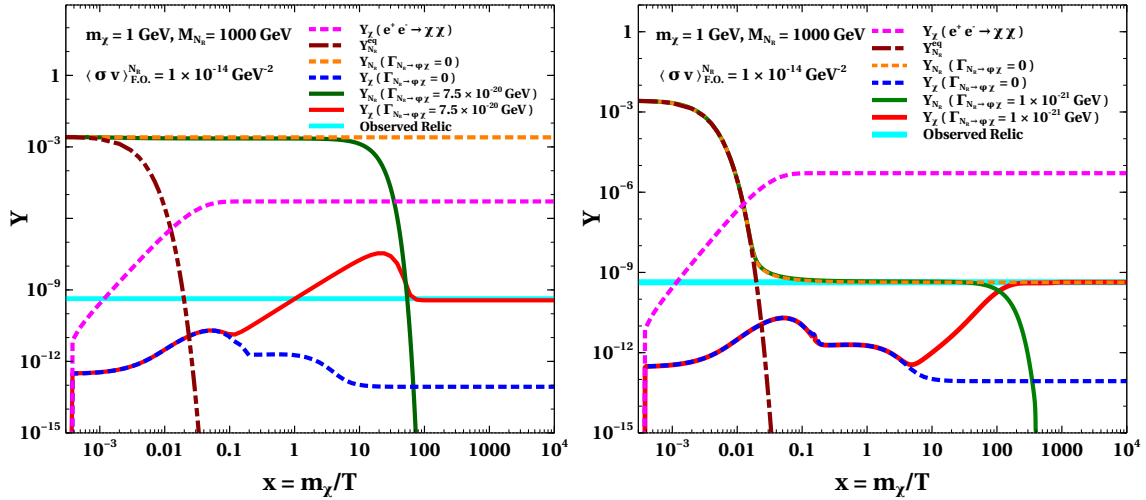


FIG. 10: (Left: Case-I, Right: Case-II.) Comoving number densities of dark sector particles considering different sub-processes indicated in the legends.

Case-II: When $\langle \sigma v \rangle_{\text{F.O.}}^{N_R}$ is such that the freeze-out abundance of N_R exactly matches the

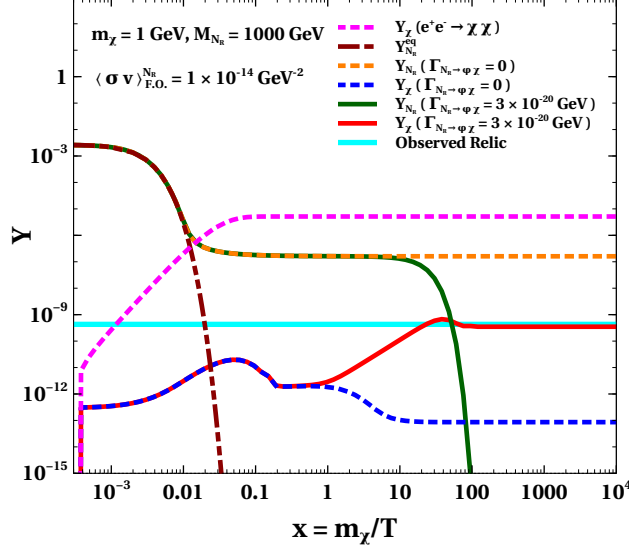


FIG. 11: (Case-III) Comoving number densities of dark sector particles considering different subprocesses indicated in the legends.

correct DM relic for a particular DM mass m_χ , the decay of N_R must occur at sufficiently late epochs² so that $\chi\chi \rightarrow Z'Z'$ remains almost ineffective when N_R abundance gets converted into DM abundance. For example, the point marked as B in the left panel of Fig. 9 indicates such a scenario for $N_R = 1000$ GeV and $m_\chi = 1$ GeV where the freeze-out abundance of N_R due to its annihilation cross-section $\langle \sigma v \rangle_{F.O.}^{N_R} = 5.6 \times 10^{-12} \text{ GeV}^{-2}$ exactly matches the required relic for a 1 GeV DM (4.4×10^{-10} in terms of comoving number density). For this particular cross-section, the decay width $\Gamma_{N_R \rightarrow \phi\chi} \leq 1 \times 10^{-21} \text{ GeV}$ while satisfying lifetime bound from BBN limits. This upper bound on decay width of N_R arises because for larger decay width and hence shorter lifetime, N_R will convert to DM at early epochs when DM annihilation into Z' pairs remain efficient further depleting its relic abundance. We show this explicitly in right panel of Fig 10, to be discussed later.

Case-III: If the N_R freeze-out cross-section $\langle \sigma v \rangle_{F.O.}^{N_R}$ has some intermediate values in between the ones mentioned in case-I and case-II above, correct relic can be obtained by a suitable combination of $\langle \sigma v \rangle_{F.O.}^{N_R}$ and $\Gamma_{N_R \rightarrow \phi\chi}$. As the cross-section gradually increases along x-axis in the left panel of Fig. 9, decoupling of N_R from the equilibrium is also delayed leading

² However, decay width can not be arbitrarily small as the decay must occur before the big bang nucleosynthesis (BBN) epoch in order to avoid extra entropy injection. Considering epoch of BBN to be around 1 sec, we get a conservative lower bound on the decay width as $\Gamma_{N_R \rightarrow \phi\chi} > 6.5 \times 10^{-25} \text{ GeV}$.

to decrease in freeze-out relic of N_R . Therefore, in order to get correct DM relic, decay of N_R should also be delayed gradually (or $\Gamma_{N_R \rightarrow \phi\chi}$ should be smaller) so that $\chi\chi \rightarrow Z'Z'$ becomes less effective by the time the decay occurs. As an example, we show in Fig. 11, the case of $\langle\sigma v\rangle_{\text{F.O.}}^{N_R} = 1 \times 10^{-14} \text{ GeV}^{-2}$ for $M_R = 1000 \text{ GeV}$, which is significantly higher than the one in case-I but lower than the one in case-II discussed above. One can see that, in order to get the correct DM relic for a 1 GeV DM, the required decay width $\Gamma_{N_R \rightarrow \phi\chi} = 3 \times 10^{-20} \text{ GeV}$ turns out to be smaller (bigger) than the ones in case-I (case-II) depicted in the left (right) panel of Fig. 10.

Thus, Fig. 9 explains the role of freeze-out cross section $\langle\sigma v\rangle_{\text{F.O.}}^{N_R}$ and decay width $\Gamma_{N_R \rightarrow \phi\chi}$ of N_R in generating the relic abundance of DM. In order to see the dependence on N_R mass, we show two different benchmark values of N_R mass namely $M_{N_R} = 100 \text{ GeV}$ and $M_{N_R} = 1000 \text{ GeV}$. When N_R mass decreases by a factor of 10, the required freeze-out cross section, increases by same factor to generate required relic of DM having mass 1 GeV, as seen from comparison of points marked as B ($m_\chi = 1 \text{ GeV}$, $M_{N_R} = 1000 \text{ GeV}$ and $\langle\sigma v\rangle_{\text{F.O.}}^{N_R} = \mathcal{O}(10^{-11}/\text{GeV}^2)$) and B' ($m_\chi = 1 \text{ GeV}$, $M_{N_R} = 100 \text{ GeV}$ and $\langle\sigma v\rangle_{\text{F.O.}}^{N_R} = \mathcal{O}(10^{-10}/\text{GeV}^2)$) on left panel of Fig. 9. Such small decay width regime requires freeze-out abundance of N_R to be finely tuned to the required DM abundance, as seen from the right panel plot of Fig. 10. Since freeze-out number density of N_R is inversely proportional to its mass as well as freeze-out cross section, one can understand the increase in freeze-out cross section while moving from point B to B' on the left panel plot of Fig. 9. On the other hand, if we focus on the region with low freeze-out cross section, the contours for $M_{N_R} = 1000 \text{ GeV}$ and $M_{N_R} = 100 \text{ GeV}$ merge with each other. This is simply because, for such low freeze-out cross-section, N_R abundance will be much more than DM abundance and hence the required DM relic can be generated only by ensuring subsequent DM annihilation into Z' pairs. This also reduces the dependence of final DM relic on freeze-out cross section as evident from the horizontal portion of the contours on left panel plot of Fig. 9. This feature is also shown on left panel plot of Fig. 10 in terms of the red solid line representing the evolution of comoving DM number density. On the left panel plot of Fig. 9, the point marked as $A(A')$ on the cyan (green) coloured line corresponds to that value of freeze-out cross-section below which the correct DM relic can be generated by the same decay width at that point. However, the freeze-out cross section can not be arbitrarily lower, as N_R needs to be thermally produced in the universe. Similar behaviour is noticed for a larger value of DM mass $m_\chi = 10 \text{ GeV}$

as shown by blue and red dashed lines on the left panel plot of Fig. 9. Compared to lighter DM, here the contours shift towards up and right, if N_R mass is kept fixed. This is primarily because for heavier DM, the required number density is less and hence a larger freeze-out cross section of N_R is also consistent in the rightmost part of the plot. For small freeze-out cross section, the corresponding decay width also becomes more (compared to the ones for lighter DM) because, heavy DM annihilation into Z' pairs will become inefficient at earlier epochs and hence it is important to ensure that N_R decays into DM at much earlier epoch. The points marked as C, C' can be understood in an analogous manner to points marked as B, B' discussed above. On the right panel plot of Fig. 9, we show the allowed region in $M_{N_R} - \langle \sigma v \rangle_{\text{F.O.}}^{N_R}$ plane by considering fixed $N_R - \chi$ coupling $y = 10^{-10}$ and DM mass $m_\chi = 1$ GeV. The behaviour can be understood in a way similar to the left panel plot, by noting that the decay width of N_R is proportional to its mass.

Now, let us discuss Fig. 10, 11 mentioned earlier where we show the evolution of comoving number densities of different species for three cases. The magenta dashed lines in all these figures show the freeze-in production of DM from the SM bath (electrons, for example) without considering any other processes like subsequent DM annihilation, RHN decay. This occurs due to the kinetic mixing of Z' with SM gauge bosons and we choose the corresponding parameter to be $\epsilon = 10^{-9}$. While DM abundance from freeze-in is huge compared to observed relic, incorporating subsequent DM annihilation into Z' pairs leads to much smaller DM relic, shown by the blue dashed lines. Due to the competing processes of DM production from freeze-in and subsequent DM annihilations, the blue dashed lines show rise, fall as well as plateau regions followed by a dark sector freeze-out around $x \sim 13$ leaving a saturated but under-abundant DM relic shown by the blue dashed line at large values of x^3 . On the other hand, N_R can be produced in equilibrium from the SM bath at very early epochs with the brown dashed line showing its equilibrium abundance, while the orange dashed line indicates its freeze-out abundance, leaving a sizeable relic depending on $\langle \sigma v \rangle_{\text{F.O.}}^{N_R}$. At late epochs N_R decays into DM filling the deficit in DM relic with the corresponding depletion in N_R abundance is shown by the solid green line. The corresponding increase in DM abundance is shown by the solid red line in Fig. 10, 11.

³ It is to be noted that since DM annihilation into light mediator is very large, final abundance after dark sector freeze-out does not significantly depends on initial freeze-in abundance from processes like $e^+e^- \rightarrow \chi\chi$ (which is proportional to ϵ^2).

C. Direct Detection

Direct detection of dark matter χ is possible through elastic scattering of χ with the nucleons of the detector atoms through $Z - Z'$ kinetic mixing⁴ as shown in Fig. 12. The Feynman diagram for the spin independent direct search cross section for a given nucleus N with proton number Z and mass number A is given by

$$\sigma_{\chi N}^{\text{SI}} = \frac{g^2 g_D^2 \epsilon^2 \mu_{\chi N}^2 (Z f_p + (A - Z) f_n)^2}{\pi M_{Z'}^4 A^2}. \quad (16)$$

Here, $\mu_{\chi N} = \frac{m_\chi m_N}{(m_\chi + m_N)}$ is the reduced mass of the DM-nucleus system, ϵ is the $Z - Z'$ kinetic mixing, f_p and f_n are the interaction strengths for proton and neutron respectively. As mentioned earlier, DM direct search experiments like CRESST-III [71] and

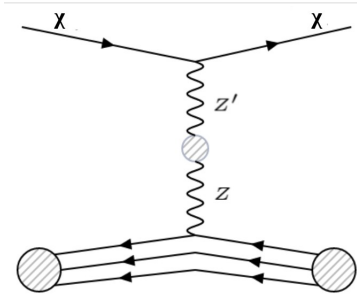


FIG. 12: Elastic scattering of DM χ off a nucleon mediated by $Z - Z'$ mixing.

XENON1T [72] can constrain the model parameters. While XENON1T provides the most stringent bound for DM of mass above 10 GeV, CRESST constraints the below 10 GeV mass range. In Fig. 13, the most stringent constraints from CRESST-III [71], XENON1T [72] experiments on $m_\chi - m_{Z'}$ plane are shown against the parameter space favoured from required DM self-interactions by assuming $\alpha_D = 0.01$. The left panel plot of Fig. 13 shows the case of attractive self-interaction while the right panel shows repulsive one. The blue coloured contours denote exclusion limits from XENON1T experiment for specific kinetic mixing parameters such that the region towards the left of the contour is excluded. Similarly, the red coloured contours show the CRESST-III bound on low mass DM for different kinetic mixing parameters ruling out the parameter space towards left of each contour.

⁴ Since kinetic mixing is between $U(1)_D$ and $U(1)_Y$, Z' can mix with photon as well but we consider $Z-Z'$ only due to larger Z coupling of SM.

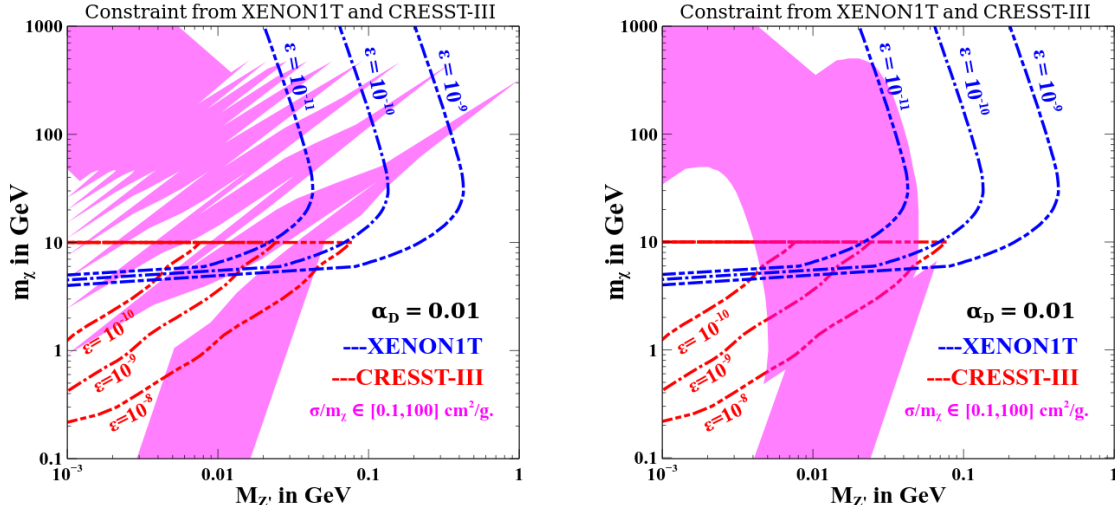


FIG. 13: Constraints from DM direct detection in the plane of DM mass (m_χ) versus mediator mass ($M_{Z'}$) for attractive (left panel) and repulsive (right panel) self-interactions respectively.

D. Summary: Minimal Setup

In Fig. 14, we summarize the parameter space in $g_D - M_{Z'}$ plane for two benchmark DM masses $m_\chi = 1$ GeV, $m_\chi = 10$ GeV on left and right panels respectively. The upper left and lower right regions are disfavoured as they give rise to too large and too small DM self-interactions respectively, leaving a band in between. Very light Z' below a few MeV is ruled out from cosmological constraints on effective relativistic degrees of freedom [5, 75–77]. This constraint has been shown by the Magenta shaded region in Fig. 15. This arises due to the late decay of such light gauge bosons into SM leptons, after standard neutrino decoupling temperatures thereby enhancing N_{eff} . We also showcase the parameter space sensitive to the future sensitivity of CMB-S4 experiment [76, 78]. This constraint has also been shown in Fig. 14 by the dark blue dotted line. In Fig. 14, a small portion of the upper left triangular region in left panel plot is disfavoured by CRESST-III bound on low mass DM while a large portion of the right panel plot is ruled out by XENON1T bound for fixed kinetic mixing $\epsilon = 10^{-10}$. The blue and red dotted lines in the left panel depicts the projected sensitivity of SuperCDMS [79] and DarkSide-LM [80] for DM mass 1 GeV and similarly the green dotted line in the right panel plot shows the projected sensitivity of XENON-nT [81] experiment for DM mass 10 GeV [82]. Since DM relic can be satisfied independently by fixing parameters related to RHN, it does not impose any further constraints in the plots shown in Fig. 14.

Since late DM annihilations produce Z' pairs copiously, we apply a conservative bound on Z' lifetime to be less than typical BBN epoch so as not to disturb the predictions of light nuclei abundance by injecting entropy. In Fig. 15, kinetic mixing parameter ϵ is shown against $M_{Z'}$. Very small kinetic mixing (the cyan coloured region) is disfavoured from this conservative lifetime bound. The chosen benchmark values of ϵ in above discussion and results automatically satisfy this lower bound. Note that due to large gauge coupling, decay of $\phi \rightarrow Z'Z'$ happens well before BBN. The decay width of these processes are summarized in Appendix A.

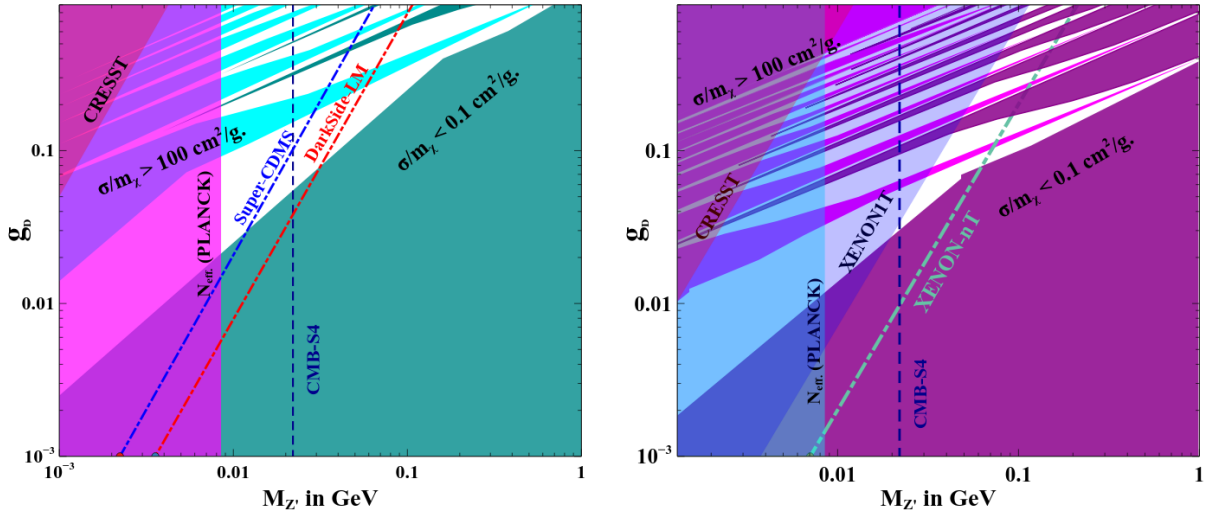


FIG. 14: Summary plot showing parameter space in $g_D - M_{Z'}$ plane for $m_\chi = 1$ GeV (left) and $m_\chi = 10$ GeV (right).

It should be noted that we are considering the kinetic mixing parameter ϵ to be a free parameter in the above discussion. However, it can be generated at one-loop level as well. There are only two particles namely χ, Φ which are charged under $U(1)_D$ and out of them, the DM χ does not have any direct coupling to SM particles. Therefore, the radiative generation of kinetic mixing is possible via scalar loop, suppressed by singlet scalar mixing with the SM Higgs $\theta_{\phi h}$ as [83, 84]

$$\epsilon_{1\text{loop}} \propto \frac{g_D g_Y}{16\pi^2} \theta_{\phi h}^2, \quad (17)$$

where g_Y is the corresponding $U(1)_Y$ gauge coupling. Since the rest of the phenomenology does not depend upon singlet-SM Higgs mixing, we can tune it arbitrarily to keep the

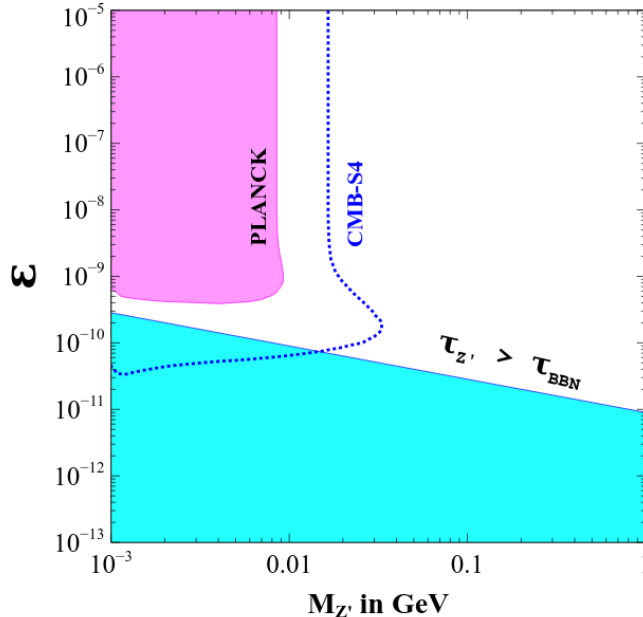


FIG. 15: Kinetic mixing parameter ϵ versus Z' mass showing the region of parameter space where Z' can be long-lived and decay after BBN. The magenta region shows the region of parameter space excluded from cosmological constraints on effective relativistic degrees of freedom. The Blue line shows the projected sensitivity of CMB-S4 experiment[76, 78].

one-loop kinetic mixing suppressed compared to the leading order value considered in the numerical analysis.

In addition to the DM phenomenology discussed above, the singlet scalar Φ can also have interesting phenomenology. While it does not couple to the SM fields directly, it can do so via its mixing with the SM Higgs. For light Z' masses and order one gauge coupling g_D , the singlet scalar VEV is expected to be of similar order as the $M_{Z'}$ resulting in light mass of the physical singlet scalar. If the singlet scalar has sizeable mixing with the SM Higgs, it can be produced in thermal bath. Since the Yukawa coupling for $N_R - \chi$ interaction with Φ is considered to be tiny for late decay of N_R , one can also have freeze-in production of DM via scalar portal interactions. In the above discussion, we have considered only gauge portal channels to be the dominant production channel for DM for simplicity and adding scalar portal interactions should not change the phenomenology significantly. The light singlet scalar can of course have other interesting phenomenology which can be probed at experiments [85].

As discussed above, the Yukawa coupling of DM with heavier RHNs ($N_{2,3}$) are assumed

to be absent for simplicity although the symmetries of the model can not forbid them. Considering them to be non-zero but as small as N_1 coupling will not make any difference to the results as $N_{2,3}$ are required to have larger Yukawa couplings with leptons from neutrino mass constraints and hence they will decay into SM particles preferentially. Considering large Yukawa couplings of $N_{2,3}$ with DM can, however, lead to thermal production of DM. But since DM continues to annihilate strongly into Z' pairs, the late decay of N_1 is still required to fill up the thermal deficit, keeping the overall scenario similar to what we have discussed here.

III. UV COMPLETE REALIZATION: TWO SCENARIOS

After discussing the phenomenology of right handed neutrino portal self-interacting DM, we now outline two specific UV complete realizations which can not only give rise to required RHN thermal abundance but also connects to the origin of light neutrino masses. We impose the constraints on RHN abundance from self-interacting DM relic criteria and find the specific model parameter space. We also compare them with existing experimental constraints and check their verifiability in near future experiments at different frontiers.

A. Scotogenic Realization

We first consider the implementation of RHN portal SIDM scenario along with the scotogenic model. As proposed by Ma in 2006 [86], scotogenic model is an extension of the SM by three copies of RHNs and an additional scalar doublet η all of which are odd under an in-built Z_2 symmetry. While the SM fields remain even under Z_2 , it is still possible for SM lepton doublets to couple to η and RHNs giving rise to the possibility of radiative neutrino masses. The BSM particle content of the model are shown in table II. Apart from the usual Z_2 and $U(1)_D$ sectors, note that the fermion DM χ is also odd under Z_2 symmetry in order to allow its RHN portal coupling with singlet scalar Φ .

The relevant Lagrangian for neutrino mass generation consistent with the imposed symmetry can be written as

$$\mathcal{L} \supset -\frac{1}{2}M_{N_R}\overline{N_R^c}N_R - Y_N\overline{L}\tilde{\eta}N_R + \text{h.c.} \quad (18)$$

Fields		$SU(3)_c \otimes SU(2)_L \otimes U(1)_Y \otimes U(1)_D \otimes Z_2$
Fermion	N_R	1 1 0 0 -
	χ	1 1 0 1 -
Scalars	η	1 2 1 0 -
	Φ	1 1 0 -1 +

TABLE II: BSM particle content and their transformation under the chosen symmetry in scotogenic realization of RHN portal SIDM.

The scalar potential involving the new scalar doublet η is.

$$\begin{aligned}
V(H, \eta) = & -\mu_H^2 H^\dagger H + \frac{\lambda_H}{2} (H^\dagger H)^2 + \mu_\eta^2 \eta^\dagger \eta + \frac{\lambda_\eta}{2} (\eta^\dagger \eta)^2 \\
& + \lambda_{H\eta} (H^\dagger H) (\eta^\dagger \eta) + \lambda'_{H\eta} (H^\dagger \eta) (\eta^\dagger H) + \frac{\lambda''_{H\eta}}{2} [(H^\dagger \eta)^2 + (\eta^\dagger H)^2] \quad (19)
\end{aligned}$$

After the electroweak symmetry breaking (EWSB), these two scalar doublets can be written

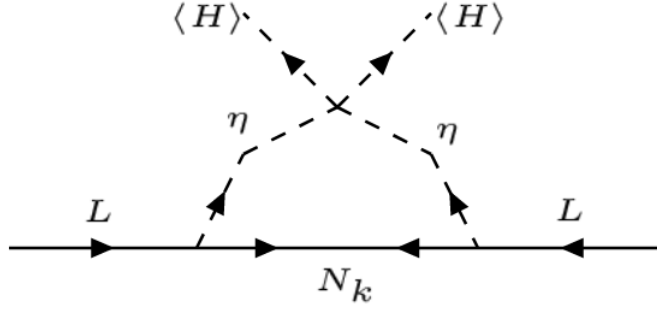


FIG. 16: Generation of one-loop neutrino mass in scotogenic model.

in unitary gauge as

$$H = \begin{pmatrix} 0 \\ \frac{v+h}{\sqrt{2}} \end{pmatrix}, \quad \eta = \begin{pmatrix} H^\pm \\ \frac{H^0 + iA^0}{\sqrt{2}} \end{pmatrix}, \quad (20)$$

where v is the VEV of SM Higgs H responsible for EWSB. The neutral scalar and pseudoscalars H^0, A^0 acquire masses as follows.

$$M_{R,I}^2 = \mu_\eta^2 + \frac{1}{2} (\lambda_{H\eta} + \lambda'_{H\eta} \pm \lambda''_{H\eta}) v^2, \quad (21)$$

with $+(-)$ denoting scalar (pseudoscalar). And the neutrino mass induced via the one-loop

diagram as shown in Fig. 16 is given by

$$(\mathcal{M}_\nu)_{\alpha\beta} = \sum_{k=1}^3 \frac{(Y_N)_{k\beta}(Y_N)_{k\alpha}}{32\pi^2} M_{N_k} \left[\frac{M_R^2}{M_R^2 - M_{N_k}^2} \ln \left(\frac{M_R^2}{M_{N_k}^2} \right) - \frac{M_I^2}{M_I^2 - M_{N_k}^2} \ln \left(\frac{M_I^2}{M_{N_k}^2} \right) \right] \quad (22)$$

where M_{N_k} is the mass eigenvalue of the RHN mass eigen-state N_k in the internal line and the indices $\alpha, \beta = e, \mu, \tau$ run over the three neutrino generations. Neutrino mass vanishes in the limit of $\lambda''_{H\eta} \rightarrow 0$ as it corresponds to degenerate neutral scalar and pseudoscalar masses $M_R^2 = M_I^2$. Thus, apart from the Yukawa coupling Y_N and RHN masses, this quartic coupling also play significant role in neutrino mass generation. To include the constraints from light neutrino data in the analysis, it is often convenient to write the Yukawa couplings in Casas-Ibarra parametrisation [87, 88] as

$$Y = \sqrt{\Lambda}^{-1} R \sqrt{\hat{m}_\nu} U_{\text{PMNS}}^\dagger \quad (23)$$

where R is an arbitrary complex orthogonal matrix satisfying $RR^T = \text{I}$ that can be parameterized in terms of three complex angles (α, β, γ) . Here, $\hat{m}_\nu = \text{Diag}(m_1, m_2, m_3)$ is the diagonal light neutrino mass matrix and the diagonal matrix Λ is defined as $\Lambda = \text{Diag}(\Lambda_1, \Lambda_2, \Lambda_3)$, with

$$\Lambda_k = \frac{M_{N_k}}{32\pi^2} \left[\frac{M_R^2}{M_R^2 - M_{N_k}^2} \ln \left(\frac{M_R^2}{M_{N_k}^2} \right) - \frac{M_I^2}{M_I^2 - M_{N_k}^2} \ln \left(\frac{M_I^2}{M_{N_k}^2} \right) \right]. \quad (24)$$

U_{PMNS} is the usual Pontecorvo-Maki-Nakagawa-Sakata (PMNS) mixing matrix of neutrinos.

1. Lightest RHN Abundance

To realize the RHN portal SIDM scenario within the scotogenic framework, we consider the lightest RHN (N_1) to be lighter than η so that it can not decay into the SM particles. And since N_1 coupling with SIDM is fine-tuned, it can be long-lived. Thus, although N_1 is not DM in our model, it can still undergo thermal freeze-out leaving a relic which later gets converted into actual DM, in a way similar to super-WIMP DM scenario [68]. As discussed in subsection II B, for a particular benchmark of SIDM parameter space, one requires a certain freeze-out abundance of N_1 so that correct SIDM relic abundance is generated at the end from non-thermal decay of N_1 . Therefore, we estimate the thermal freeze-out abundance of N_1 in the scotogenic model in a way similar to fermion DM studies in scotogenic model [89–91].

Since N_1 interacts with the SM bath only via Yukawa couplings, one requires sizeable Yukawas in order to generate the required thermal relic. Unlike in conventional seesaw models at low scale, scotogenic model offers the possibility to have sizeable Yukawa couplings and still satisfy the light neutrino mass because of the loop suppression involved and the freedom to choose the scalar quartic coupling. Depending upon the size of Yukawa couplings as well as mass splitting with other Z_2 odd particles, required N_1 abundance can be generated due to dominance of usual annihilation, coannihilation [92] or a combination of both. And these Yukawa couplings are essentially instrumental in keeping the RHNs in thermal equilibrium in early universe which then decouples and decays to DM χ and ϕ to generate the correct DM relic through a non-thermal mechanism as discussed in section II B. While singlet RHNs are not constrained from collider searches, the requirement of large Yukawa couplings can lead to some tensions with other experimental bounds like charged lepton flavour violation which we discuss below.

2. Lepton flavour violation

In the SM, charged lepton flavour violating (CLFV) decays occurs at loop level and is highly suppressed by the smallness of neutrino masses, and thus is much beyond the current experimental sensitivity [93]. Therefore, any future observation of such LFV decays like $\mu \rightarrow e\gamma$ will definitely be an indication of new physics beyond the SM.

In the scotogenic model, the charged component of the additional scalar doublet η going inside a loop along with singlet fermions can facilitate such CLFV decays.

$\mu \rightarrow e\gamma$

Following the prescriptions given in [88, 94], the decay width of $\mu \rightarrow e\gamma$ can be calculated as

$$\text{Br}(\mu \rightarrow e\gamma) = \frac{3(4\pi)^3\alpha}{4G_F^2} |A_D|^2 \text{Br}(\mu \rightarrow e\nu_\mu\bar{\nu}_e), \quad (25)$$

where A_D is given by

$$A_D = \sum_k \frac{(Y_N)_{ke}^*(Y_N)_{k\mu}}{16\pi^2} \frac{1}{M_{\eta^+}^2} f(r_k), \quad (26)$$

with $r_k = M_{N_k}^2/M_{\eta^+}^2$. $f(x)$ is the loop function given by

$$f(x) = \frac{1 - 6x + 3x^2 + 2x^3 - 6x^2 \log x}{12(1-x)^4}. \quad (27)$$

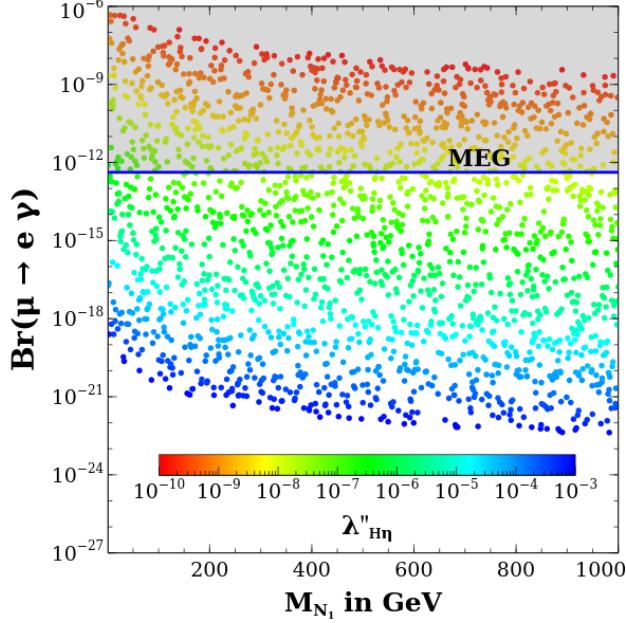


FIG. 17: $\text{Br}(\mu \rightarrow e\gamma)$ as a function of N_1 mass while keeping $M_{N_1} = M_{N_2} - 10 \text{ GeV} = M_{N_3} - 20 \text{ GeV}$, $M_{\eta^+} = 1 \text{ TeV}$.

The latest bound from the MEG collaboration is $\text{Br}(\mu \rightarrow e\gamma) < 4.2 \times 10^{-13}$ at 90% confidence level [93]. In Fig. 17, $\text{Br}(\mu \rightarrow e\gamma)$ is shown as a function of N_1 mass. For the scan, we fixed the mass splitting between N_1 with N_2 and N_3 at 10 GeV and 20 GeV respectively and fixed charged scalar η^+ mass at 1 TeV. Here considering the normal ordering, the lightest active neutrino mass is assumed to be 10^{-3} eV consistent with the constraint for the sum of active neutrino masses $\sum m_\nu = 0.12 \text{ eV}$ from cosmological data. The solid Blue line represents the latest upper limit from the MEG experiment. It is clear that $\lambda''_{H\eta}$ smaller than $\sim \mathcal{O}(10^{-8})$ is disfavoured from the CLFV constraint consequently putting an upper limit on the Yukawa couplings.

$\mu \rightarrow 3e$

In addition to $\mu \rightarrow e\gamma$, another CLFV observable that can provide distinctive signature is the three body decay process $\mu \rightarrow 3e$. This branching fraction is given by [88]:

$$\begin{aligned} \text{Br}(\mu \rightarrow e\bar{e}e) = & \frac{3(4\pi)^2 \alpha_{\text{em}}^2}{8G_F^2} \left[|A_{ND}|^2 + |A_D|^2 \left(\frac{16}{3} \log\left(\frac{m_\mu}{m_e}\right) - \frac{22}{3} \right) + \frac{1}{6}|B|^2 \right. \\ & \left. + \frac{1}{3}(2|F_{RR}|^2 + |F_{RL}|^2) + \left(-2A_{ND}A_D^* + \frac{1}{3}A_{ND}B^* - \frac{2}{3}A_DB^* + \text{h.c.} \right) \right] \\ & \times \text{Br}(\mu \rightarrow e\nu_\mu\bar{\nu}_e) \end{aligned} \quad (28)$$

where A_D is as given in Eq. 26, and A_{ND} is given by:

$$A_{ND} = \sum_{k=1}^3 \frac{(Y_N)_{ke}^* (Y_N)_{k\mu}}{6(4\pi)^2} \frac{1}{M_{\eta^+}^2} G_2(r_k), \quad (29)$$

and

$$F_{RR} = \frac{F g_R^\ell}{g_2^2 \sin^2 \theta_W M_Z^2}, \quad F_{RL} = \frac{F g_L^\ell}{g_2^2 \sin^2 \theta_W M_Z^2}, \quad (30)$$

with the co-efficient F given by

$$F = \sum_{k=1}^3 \frac{(Y_N)_{ke}^* (Y_N)_{k\mu}}{2(4\pi)^2} \frac{m_\mu m_e}{M_{\eta^+}^2} \frac{g_2}{\cos \theta_W} F_2(r_k). \quad (31)$$

For the Box diagrams, the co-efficient B is given by:

$$B = \frac{1}{(4\pi)^2 e^2 M_{\eta^+}^2} \sum_{j,k=1}^3 \left[\frac{1}{2} D_1(r_j, r_k) (Y_N)_{ke}^* (Y_N)_{ke} (Y_N)_{je}^* (Y_N)_{j\mu} + \sqrt{r_j r_k} D_2(r_j, r_k) (Y_N)_{ke}^* (Y_N)_{ke}^* (Y_N)_{je} (Y_N)_{j\mu} \right]. \quad (32)$$

The loop functions G_2, F_2, D_1, D_2 are given in Appendix B.

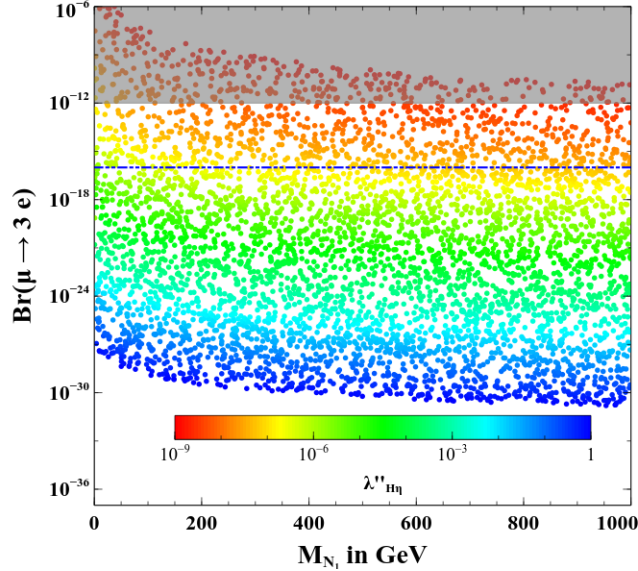


FIG. 18: $\text{Br}(\mu \rightarrow 3e)$ as a function of N_1 mass while keeping $M_{N_1} = M_{N_2} - 10 \text{ GeV} = M_{N_3} - 20 \text{ GeV}$, $M_{\eta^+} = 1 \text{ TeV}$. The grey shaded region shows the present bound [95] and the blue dotted line shows the future sensitivity. [96]

$\mu \rightarrow e$ conversion in nuclei

Because of the great projected sensitivities of various collaborations, $\mu \rightarrow e$ conversion in nuclei might become the most severely constrained observable in scotogenic scenarios. The

conversion rate, relative to the the muon capture rate, can be expressed as:

$$\begin{aligned} \text{CR}(\mu - e, \text{Nucleus}) &= \frac{p_e E_e m_\mu^3 G_F^2 \alpha_{\text{em}}^3 Z_{\text{eff}}^4 F_p^2}{8 \pi^2 Z} \\ &\times \left\{ \left| (Z + N) \left(g_{LV}^{(0)} + g_{LS}^{(0)} \right) + (Z - N) \left(g_{LV}^{(1)} + g_{LS}^{(1)} \right) \right|^2 + \right. \\ &\quad \left. \left| (Z + N) \left(g_{RV}^{(0)} + g_{RS}^{(0)} \right) + (Z - N) \left(g_{RV}^{(1)} + g_{RS}^{(1)} \right) \right|^2 \right\} \frac{1}{\Gamma_{\text{capt}}} . \quad (33) \end{aligned}$$

where Z and N are the number of protons and neutrons in the nucleus, Z_{eff} is the effective atomic charge, F_p is the nuclear matrix element and Γ_{capt} represents the total muon capture rate. Furthermore, p_e and E_e (taken to be $\simeq m_\mu$ in the numerical evaluation) are the momentum and energy of the electron and m_μ is the muon mass. The other couplings can be found in Appendix C.

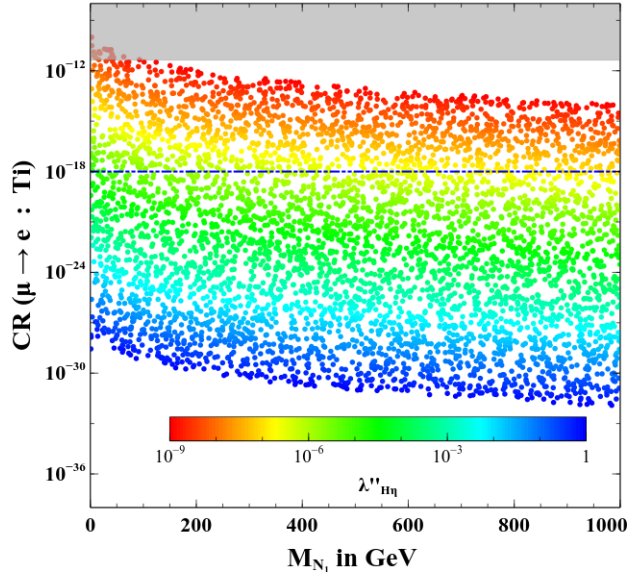


FIG. 19: $\text{CR}(\mu \rightarrow e : \text{Ti})$ as a function of N_1 mass while keeping $M_{N_1} = M_{N_2} - 10 \text{ GeV} = M_{N_3} - 20 \text{ GeV}$, $M_{\eta^+} = 1 \text{ TeV}$. The grey shaded region shows the present bound [97] and the blue dotted line shows the future sensitivity. [96]

Having studied all these CLFV processes, finally we show the scotogenic model parameter space consistent with SIDM relic criteria in left panel of Fig. 20 in the plane of N_1 Yukawa and its mass. As mentioned earlier, for a fixed range or value of SIDM parameters, we have a constraint on the cross-section $\langle \sigma v \rangle_{\text{F.O.}}^{N_1}$ such that the required N_1 freeze-out abundance is generated which later gets transferred into SIDM χ . In this figure, the points in blue, cyan and pink coloured dots are allowed from CLFV bounds while the grey coloured box shaped

points which do not overlap with the coloured points are disallowed. This clearly shows that the model parameters consistent with SIDM relic remains verifiable at ongoing experiments. In the right panel of Fig. 20, the contours of correct DM relic in the plane of $\langle\sigma v\rangle_{\text{F.O.}}^{N_1}$ and $\Gamma_{N_1\rightarrow\phi\chi}$ are shown for $M_{N_1} = 100$ GeV and $m_\chi = 1, 10$ GeV similar to the left panel plot of Fig. 9. Here the magenta shaded region depicts the region disfavoured by CLFV bounds from the MEG experiment [93] which is the most stringent among all CLFV constraints. Since the freeze-out cross-section of N_1 depends upon its Yukawa couplings with leptons, the disfavoured region corresponds to large cross section and hence large Yukawa couplings which give a very large CLFV rate disfavoured by experimental bounds. For this analysis, we have ignored the co-annihilation effects by maintaining a minimum mass difference of 100 GeV between lightest RHN (N_1) and the doublet scalar η . However we have checked that if this mass-difference is below 30 GeV, then it can enhance the effective freeze-out cross-section of N_1 because of co-annihilations relaxing the dependence as well as bound on the Yukawa couplings. If N_1 mass is fixed at 100 GeV along with the Yukawa coupling y such that the decay $\Gamma_{N_1\rightarrow\phi\chi}$ is of the order $\mathcal{O}(10^{-20})$, then one can obtain the required freeze-out cross-section of N_1 that can lead to the correct relic of SIDM by maintaining a mass-difference of 20 – 30 GeV and 5 – 10 GeV between N_1 and η for $m_\chi = 1$ GeV, $m_\chi = 10$ GeV respectively.

B. Gauged $B - L$ realization

In this subsection, we consider another interesting UV completion of RHN portal SIDM scenario based on the gauged $B - L$ symmetry where B and L correspond to baryon and lepton numbers respectively. Since its proposal and early studies several decades ago [98–103], gauged $B - L$ scenarios have become a popular BSM framework as it addresses the problem of neutrino mass and, in some specific non-minimal realizations, can also provide a realistic dark matter candidate. Here we consider the minimal scenario based on gauged $B - L$ framework where, in addition to SM and SIDM sectors, three RHNs and one additional singlet scalar ζ are required. The BSM particle content is shown in table III. The three RHNs with $B - L$ charge -1 each also lead to cancellation of triangle anomalies keeping the model anomaly free.

The relevant Lagrangian for neutrino mass generation consistent with the imposed sym-

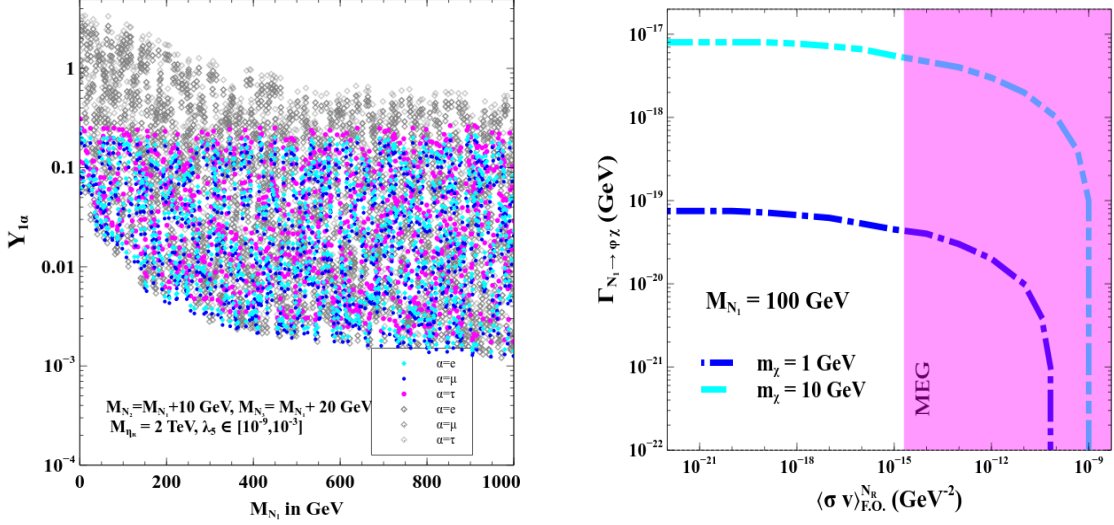


FIG. 20: [Left]:Parameter space for scotogenic model in the plane of N_1 Yukawa and its mass consistent with SIDM relic. The coloured dots (blue, cyan, pink) are allowed from CLFV bounds while the grey coloured box shaped points which do not overlap with the colored points are disallowed. [Right]: Contours of correct DM relic in the plane of $\langle \sigma v \rangle_{F.O.}^{N_1}$ and $\Gamma_{N_1 \rightarrow \phi \chi}$ where the magenta shaded region is disfavoured due to CLFV bounds from the MEG experiment.

Fields		$SU(3)_c \otimes SU(2)_L \otimes U(1)_Y \otimes U(1)_{B-L} \otimes U(1)_D$				
Fermion	N_R	1	1	0	-1	0
	χ	1	1	0	0	1
Scalars	Φ	1	1	0	1	-1
	ζ	1	1	0	2	0

TABLE III: BSM particle content and their transformation under the chosen symmetry in gauged $B - L$ realization of RHN portal SIDM.

metry is given by

$$\mathcal{L} \supset -\frac{1}{2} f \zeta \overline{N_R^c} N_R - Y_\nu \overline{L} \tilde{H} N_R + \text{h.c.} \quad (34)$$

The singlet scalar ζ , after acquiring a non-zero VEV, denoted by v_{BL} , not only lead to spontaneous breaking of gauged $B - L$ symmetry but also generated RHN mass $M_{N_R} = f v_{BL} / \sqrt{2}$. And through the Yukawa coupling, after the EWSB, the neutrinos acquire a Dirac mass which is equal to $m_D = Y_\nu v / \sqrt{2}$. Since N_R has Majorana mass M_{N_R} and also mixes with light neutrinos via Dirac mass m_D , one needs to diagonalise the mass matrix in

SM neutrino and RHN basis. Assuming a hierarchy $m_D \ll M_{N_R}$ leads to the light neutrino mass matrix via type-I seesaw mechanism as

$$M_\nu = -m_D M_{N_R}^{-1} m_D^T \quad (35)$$

which is a 3×3 complex matrix and can be diagonalised by the PMNS mixing matrix in diagonal charged lepton basis.

Now, as far as the lightest RHN N_1 acting as the portal to SIDM is concerned, there are two crucial difference between gauged $B - L$ model and scotogenic model discussed earlier. We elaborate them below.

- N_1 couples to SM leptons via SM Higgs H and hence can not be made stable kinematically against decay into SM particles. This requires the tuning of N_1 Yukawa with SM leptons such that N_1 can decay dominantly into SIDM at late epochs. Such fine-tuning of N_1 Yukawa with SM leptons lead to vanishingly small lightest neutrino mass.
- Since N_1 can have tiny couplings with the SM leptons, DM in $B - L$ model can, in principle, decay into SM neutrinos which can be constrained from different neutrino experiments, as discussed in [53]. As a conservative approach, we consider N_1 coupling with leptons to be vanishingly small in our analysis.
- Even though N_1 Yukawa with SM leptons is very small, N_1 can still be produced in the thermal bath if the gauged $B - L$ portal interactions are sizeable enough. Thus, even though the prospects of probing this scenario at LFV experiments are substantially less compared to the scotogenic realization, the gauged $B - L$ interactions can be probed at colliders.

In general both gauged $B - L$ and scalar portal interactions can be responsible for keeping the RHNs in thermal equilibrium with the SM bath in early epochs. The scalar portal interactions can arise due to mixing of ζ with the SM Higgs which we ignore in our work and constrain the gauge interactions only from the requirement of appropriate cross-section $\langle \sigma v \rangle_{N_1 N_1 \rightarrow \text{SM SM}}$ leading to a freeze-out abundance of N_1 . The gauge interactions of N_1 arise due to the kinetic terms as

$$\mathcal{L}_{\text{kinetic}} \supset i \overline{N_R} \not{D} N_R, \quad D_\mu = \partial_\mu - i g_{\text{BL}} (Z_{\text{BL}})_\mu. \quad (36)$$

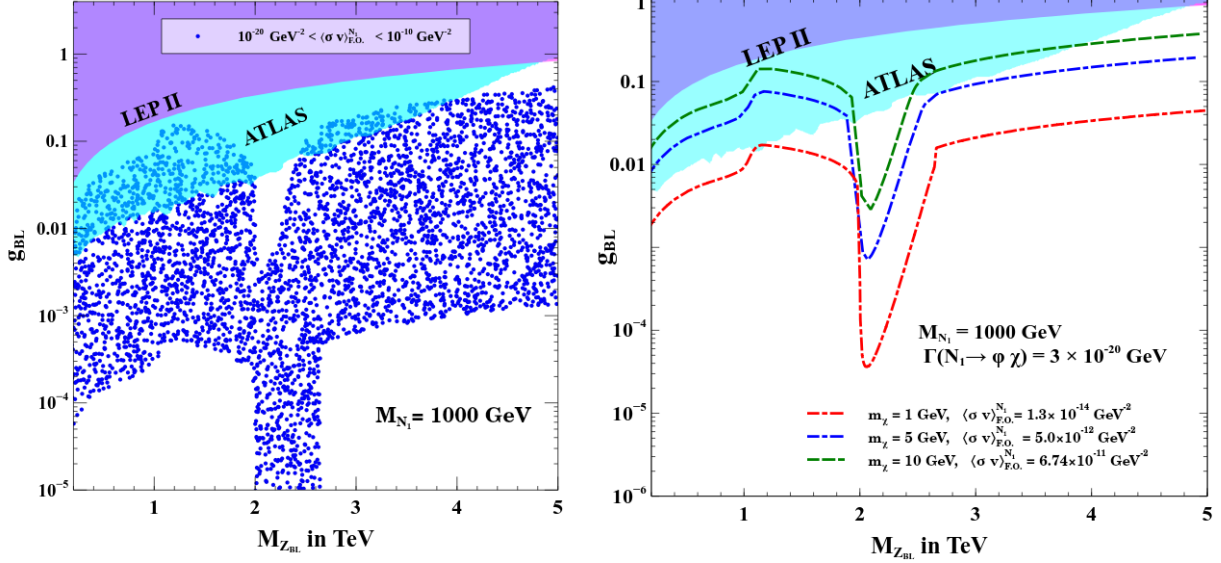


FIG. 21: Left: Parameter space for gauged $B - L$ model consistent with the required cross section of the lightest RHN in order to generate its required thermal relic, to be transferred to SIDM at late epochs.; Right: Contours of the required cross-section $\langle \sigma v \rangle_{\text{F.O.}}^{N_1}$ that can give rise to correct relic abundance for different DM masses ($m_\chi = 1, 5, 10$ GeV) with a fixed N_1 mass ($M_{N_1} = 1000$ GeV) and decay width ($\Gamma_{N_1 \rightarrow \phi \chi} = 3 \times 10^{-20}$ GeV) in the plane of $M_{Z_{BL}}$ and g_{BL} .

At late epochs, N_1 can decay into SIDM χ to fulfill the relic criteria of the latter as discussed in subsection II B. In left panel of Fig. 21, we show the parameter space in the plane of $B - L$ gauge coupling g_{BL} and the gauge boson mass $M_{Z_{BL}}$ consistent with the required N_1 annihilation cross-section or freeze-out abundance. For the scan N_1 mass was fixed at 1000 GeV and $M_{Z_{B-L}}$ was varied upto 5 TeV. Clearly we can see the resonance feature around $M_{Z_{BL}} = 2$ TeV due to dominant N_1 annihilation mediated by Z_{BL} . In the right panel of Fig. 21, we show the contours of the required N_1 annihilation cross-section in the plane of $M_{Z_{BL}}$ and g_{BL} that can give rise to correct relic abundance for different DM masses ($m_\chi = 1, 5, 10$ GeV) with a fixed N_1 mass ($M_{N_1} = 1000$ GeV) and decay width ($\Gamma_{N_1 \rightarrow \phi \chi} = 3 \times 10^{-20}$ GeV).

While we need sizeable $B - L$ gauge sector coupling with light Z_{BL} so that N_1 can attain the required freeze-out relic, the corresponding parameter space is tightly constrained from collider experiments. The limits from LEP II data constrains such additional gauge sector by imposing a lower bound on the ratio of new gauge boson mass to the new gauge coupling $M_{Z'}/g' \geq 7$ TeV [104, 105]. The bounds from ongoing LHC experiment have already

surpassed the LEP II bounds. In particular, search for high mass dilepton resonances have put strict bounds on such additional gauge sector coupling to all generations of leptons and quarks with coupling similar to electroweak ones. The latest bounds from the ATLAS experiment [106, 107] and the CMS experiment [108] at the LHC rule out such gauge boson masses below 4-5 TeV from analysis of 13 TeV data. Such bounds get weaker, if the corresponding gauge couplings are weaker [106] than the electroweak gauge couplings. We show these exclusion limits in Fig. 21. Clearly, the ATLAS limit from 13 TeV LHC data rules out some portion of the parameter space while keeping the other parts predictive at near future runs.

Here it is worth mentioning that, for a particular DM mass m_χ , if $\Gamma_{N_1 \rightarrow \phi\chi}$ is further decreased (Mass of N_1 , M_{N_1} and Yukawa coupling y can always be tuned accordingly) upto 10^{-21} GeV, then that would require a larger freeze-out cross-section $\langle\sigma v\rangle_{\text{F.O.}}^{N_1}$ so as to give rise to correct relic abundance of DM χ which can be inferred from Fig. 9. To obtain a larger freeze-out cross-section through the B – L gauge portal, one would require to have a larger gauge coupling g_{BL} . But since such larger gauge couplings are constrained from the collider experiments, so in that case some more parameter space will get ruled out. Beyond $\Gamma_{N_1 \rightarrow \phi\chi} = 10^{-21}$ GeV, if it is further decreased, then there would be no effect on the $g_{\text{BL}} - M_{Z_{\text{BL}}}$ parameter space, as the same freeze-out cross-section can lead to correct relic of χ which is explained clearly in section II B. On the contrary, if $\Gamma_{N_1 \rightarrow \phi\chi}$ is increased, then the required $\langle\sigma v\rangle_{\text{F.O.}}^{N_1}$ will decrease which can be easily achieved through the B – L gauge portal without any tension from the collider constraints from ATLAS and LEP II.

IV. CONCLUSION

We have studied a self-interacting dark matter scenario consistent with astrophysical requirements of addressing the small scale issues of cold dark matter paradigm. Due to the existence of a light mediator, considered to be the vector boson of a gauged dark Abelian symmetry, velocity-dependent DM self-interactions can be naturally realised giving rise to the required differences across astrophysical scales from dwarf galaxies to clusters. Depending upon the kinetic mixing of dark $U(1)_D$ with the SM hypercharge $U(1)_Y$, DM can be produced either thermally or non-thermally from the SM bath although the thermal scenario faces tight constraints from DM direct detection experiments. Irrespective of thermal

or non-thermal production, the final DM relic remains sub-dominant due to strong DM annihilations into its light mediators by virtue of large self-interaction coupling. In order to fill the relic deficit of SIDM, we propose a right handed neutrino portal SIDM scenario which can also have non-trivial connection to the origin of light neutrino masses depending upon the particular UV completion.

We first show the salient features of this scenario by discussing the minimal model along with DM self-interactions, DM relic via a hybrid of thermal and non-thermal mechanisms and DM direct detection. We then propose two UV complete realizations of this minimal RHN portal SIDM setup namely, scotogenic and gauged $B - L$ realizations. In scotogenic realization, in addition to SM and SIDM sectors, there exist three RHNs and an extra scalar doublet odd under an unbroken Z_2 symmetry. While light neutrino mass arises at one-loop with Z_2 -odd particles going inside the loop, the lightest RHN N_1 can acquire a freeze-out relic due to sizeable interactions with SM leptons. While N_1 decay into SM lepton is forbidden kinematically, it can decay into SIDM at late epochs thereby generating the required relic. The requirement of sizeable Yukawa couplings of N_1 also keeps the model predictive at experiments looking for charged lepton flavour violation. As a second example of UV completion, we consider another popular framework based on the gauged $B - L$ symmetry where three RHNs are also required as a minimal solution to the triangle anomaly cancellation, apart from their roles in generating light neutrino masses via type-I seesaw mechanism. While the lightest RHN decay into SM leptons can be made negligible by appropriate fine-tuning of Dirac Yukawa couplings with the consequence of vanishingly small lightest neutrino mass, the required N_1 freeze-out relic (to fill the SIDM relic deficit via late decay) can still be generated by virtue of gauged $B - L$ interactions. While the LFV prospects are low due to fine-tuned Yukawa of the lightest RHN with leptons, the model remains predictive at collider experiments due to $B - L$ interactions. Additionally, the $B - L$ framework also allows for the option of long-lived DM as there is no unbroken symmetry protecting its stability. While we did not pursue the indirect detection phenomenology of such a scenario and kept the N_1 coupling to leptons vanishingly small, such long-lived DM decaying into neutrinos can be probed at different neutrino detectors. Additionally, keeping N_1 -lepton coupling non-vanishing but comparable to N_1 -DM coupling will also involve a more rigorous treatment of relic density calculation as N_1 can simultaneously convert into radiation and DM at late epochs. We leave such interesting possibilities to future works. Finally, to sum-

marize our present work, the minimal setup of RHN portal SIDM remains predictive with respect to observations in astrophysics, cosmology and DM direct detection experiments while the specific UV completions can offer complementary probes at experiments in energy and intensity frontiers.

Acknowledgments

DB acknowledges the support from Early Career Research Award from Science and Engineering Research Board (SERB), Department of Science and Technology (DST), Government of India (reference number: ECR/2017/001873). MD acknowledges DST, Government of India for providing the financial assistance for the research under the grant DST/INSPIRE/03/ 2017/000032.

APPENDIX A: RELEVANT CROSS SECTION AND DECAY WIDTHS

$$\Gamma(N_R \rightarrow \phi\chi) = \frac{y^2}{32\pi M_{N_R}^3} \left((M_{N_R} + m_\chi)^2 - m_\phi^2 \right) \left(M_{N_R}^4 + m_\chi^4 + m_\phi^4 - 2M_{N_R}^2 m_\chi^2 - 2m_\chi^2 m_\phi^2 - 2M_{N_R}^2 m_\phi^2 \right)^{\frac{1}{2}} \quad (\text{A1})$$

$$\sigma(\chi\chi \rightarrow Z'Z') = \frac{g'^4}{192\pi s(s-4m_\chi^2)} \times \left[\frac{24s(4m_\chi^4 + 2M_{Z'}^4 + sm_\chi^2)A}{M_{Z'}^4 + m_\chi^2 s - 4M_{Z'}^2 m_\chi^2} - \frac{24(8m_\chi^2 - 4M_{Z'}^2 - s^2 - (s-2M_{Z'}^2)4m_\chi^2)}{s-2M_{Z'}^2} \text{Log} \left[\frac{2M_{Z'}^2 + s(A-1)}{2M_{Z'}^2 - s(A+1)} \right] \right] \quad (\text{A2})$$

where $A = \sqrt{\frac{(s-4M_{Z'}^2)(s-4m_\chi^2)}{s^2}}$

$$\sigma(e^+e^- \rightarrow \chi\chi) = \frac{g^2 g'^2 \epsilon^2 (s+2m_\chi^2)(s-m_e^2 - 4(s+2m_e^2)\sin^2\theta_W)}{96\pi \cos^2\theta_W (s-4m_e^2)(s-m_{Z'}^2)^2} \sqrt{\frac{(s-4m_e^2)(s-4m_\chi^2)}{s^2}} \quad (\text{A3})$$

Thermal averaged cross-section for annihilation of any particle A to B is given by: [74]

$$\langle\sigma v\rangle_{AA\rightarrow BB} = \frac{x}{2[K_1^2(x) + K_2^2(x)]} \times \int_2^\infty dz \sigma_{(AA\rightarrow BB)}(z^2 m_A^2) (z^2 - 4) z^2 K_1(zx) \quad (\text{A4})$$

where $z = \sqrt{s}/m_A$ and $x = m_A/T$.

Thermal averaged decay width of Φ_1 decaying to χ_1 is given by:

$$\langle \Gamma(\Phi_1 \rightarrow \chi_1 \chi_1) \rangle = \Gamma(\Phi_1 \rightarrow \chi_1 \chi_1) \left(\frac{K_1(x)}{K_2(x)} \right) \quad (\text{A5})$$

In Eqn. (A4) and (A5), K_1 and K_2 are the modified Bessel functions of 1st and 2nd kind respectively.

The decay width of Z' into a e^+e^- pair or pair of neutrinos:

$$\Gamma_{Z \rightarrow f\bar{f}} = \frac{\epsilon^2 g^2 M_{Z'}}{48\pi \cos^2 \theta_w} (C_{fA}^2 + C_{fV}^2) \quad (\text{A6})$$

APPENDIX B: LOOP FUNCTIONS

The loop functions used in section III A 2 are given by [88]

$$F_2(x) = \frac{1 - 6x + 3x^2 + 2x^3 - 6x^2 \log x}{6(1-x)^4}, \quad (\text{B1})$$

$$G_2(x) = \frac{2 - 9x + 18x^2 - 11x^3 + 6x^3 \log x}{6(1-x)^4}, \quad (\text{B2})$$

$$D_1(x, y) = -\frac{1}{(1-x)(1-y)} - \frac{x^2 \log x}{(1-x)^2(x-y)} - \frac{y^2 \log y}{(1-y)^2(y-x)}, \quad (\text{B3})$$

$$D_2(x, y) = -\frac{1}{(1-x)(1-y)} - \frac{x \log x}{(1-x)^2(x-y)} - \frac{y \log y}{(1-y)^2(y-x)}. \quad (\text{B4})$$

These loop functions do not have any poles. In the limit $x, y \rightarrow 1$ and $y \rightarrow x$, the functions become

$$F_2(1) = \frac{1}{12}, \quad G_2(1) = \frac{1}{4}, \quad D_1(1, 1) = -\frac{1}{3}, \quad D_2(1, 1) = \frac{1}{6}, \quad (\text{B5})$$

$$D_1(x, x) = \frac{-1 + x^2 - 2x \log x}{(1-x)^3}, \quad (\text{B6})$$

$$D_1(x, 1) = D_1(1, x) = \frac{-1 + 4x - 3x^2 + 2x^2 \log x}{2(1-x)^3}, \quad (\text{B7})$$

$$D_2(x, x) = \frac{-2 + 2x - (1+x) \log x}{(1-x)^3}, \quad (\text{B8})$$

$$D_2(x, 1) = D_2(1, x) = \frac{1 - x^2 + 2x \log x}{2(1-x)^3}. \quad (\text{B9})$$

APPENDIX C: COUPLINGS RELEVANT FOR $\mu \rightarrow e$ CONVERSION IN NUCLEI

In the above, $g_{XK}^{(0)}$ and $g_{XK}^{(1)}$ (with $X = L, R$ and $K = S, V$) are given by

$$\begin{aligned} g_{XK}^{(0)} &= \frac{1}{2} \sum_{q=u,d,s} \left(g_{XK(q)} G_K^{(q,p)} + g_{XK(q)} G_K^{(q,n)} \right), \\ g_{XK}^{(1)} &= \frac{1}{2} \sum_{q=u,d,s} \left(g_{XK(q)} G_K^{(q,p)} - g_{XK(q)} G_K^{(q,n)} \right). \end{aligned} \quad (\text{C1})$$

Neglecting the Higgs-penguin contributions due to the smallness of the involved Yukawa couplings. Therefore, the corresponding couplings are

$$\begin{aligned} g_{LV(q)} &= g_{LV(q)}^\gamma + g_{LV(q)}^Z, \\ g_{RV(q)} &= g_{LV(q)} \Big|_{L \leftrightarrow R}, \\ g_{LS(q)} &\approx 0, \\ g_{RS(q)} &\approx 0. \end{aligned} \quad (\text{C2})$$

The photon and Z -boson couplings can be computed from the Feynman diagrams which are given by:

$$\begin{aligned} g_{LV(q)}^\gamma &= \frac{\sqrt{2}}{G_F} e^2 Q_q (A_{ND} - A_D), \\ g_{RV(q)}^Z &= -\frac{\sqrt{2}}{G_F} \frac{g_L^q + g_R^q}{2} \frac{F}{M_Z^2}. \end{aligned} \quad (\text{C3})$$

And the tree-level Z -boson couplings to a pair of quarks are:

$$g_L^q = \frac{g_2}{\cos \theta_W} (Q_q \sin^2 \theta_W - T_3^q), \quad g_R^q = \frac{g_2}{\cos \theta_W} Q_q \sin^2 \theta_W, \quad (\text{C4})$$

-
- [1] F. Zwicky, *Die Rotverschiebung von extragalaktischen Nebeln*, *Helv. Phys. Acta* **6** (1933) 110–127. [Gen. Rel. Grav.41,207(2009)].
 - [2] V. C. Rubin and W. K. Ford, Jr., *Rotation of the Andromeda Nebula from a Spectroscopic Survey of Emission Regions*, *Astrophys. J.* **159** (1970) 379–403.
 - [3] D. Clowe, M. Bradac, A. H. Gonzalez, M. Markevitch, S. W. Randall, C. Jones, and D. Zaritsky, *A direct empirical proof of the existence of dark matter*, *Astrophys. J.* **648** (2006) L109–L113, [[astro-ph/0608407](https://arxiv.org/abs/astro-ph/0608407)].

- [4] **Particle Data Group** Collaboration, P. A. Zyla et al., *Review of Particle Physics*, *PTEP* **2020** (2020), no. 8 083C01.
- [5] **Planck** Collaboration, N. Aghanim et al., *Planck 2018 results. VI. Cosmological parameters*, [arXiv:1807.06209](#).
- [6] E. W. Kolb and M. S. Turner, *The Early Universe*, vol. 69. 1990.
- [7] S. Tulin and H.-B. Yu, *Dark Matter Self-interactions and Small Scale Structure*, *Phys. Rept.* **730** (2018) 1–57, [[arXiv:1705.02358](#)].
- [8] J. S. Bullock and M. Boylan-Kolchin, *Small-Scale Challenges to the Λ CDM Paradigm*, *Ann. Rev. Astron. Astrophys.* **55** (2017) 343–387, [[arXiv:1707.04256](#)].
- [9] D. N. Spergel and P. J. Steinhardt, *Observational evidence for selfinteracting cold dark matter*, *Phys. Rev. Lett.* **84** (2000) 3760–3763, [[astro-ph/9909386](#)].
- [10] E. D. Carlson, M. E. Machacek, and L. J. Hall, *Self-interacting dark matter*, *Astrophys. J.* **398** (1992) 43–52.
- [11] A. A. de Laix, R. J. Scherrer, and R. K. Schaefer, *Constraints of selfinteracting dark matter*, *Astrophys. J.* **452** (1995) 495, [[astro-ph/9502087](#)].
- [12] M. R. Buckley and P. J. Fox, *Dark Matter Self-Interactions and Light Force Carriers*, *Phys. Rev. D* **81** (2010) 083522, [[arXiv:0911.3898](#)].
- [13] J. L. Feng, M. Kaplinghat, and H.-B. Yu, *Halo Shape and Relic Density Exclusions of Sommerfeld-Enhanced Dark Matter Explanations of Cosmic Ray Excesses*, *Phys. Rev. Lett.* **104** (2010) 151301, [[arXiv:0911.0422](#)].
- [14] J. L. Feng, M. Kaplinghat, H. Tu, and H.-B. Yu, *Hidden Charged Dark Matter*, *JCAP* **07** (2009) 004, [[arXiv:0905.3039](#)].
- [15] A. Loeb and N. Weiner, *Cores in Dwarf Galaxies from Dark Matter with a Yukawa Potential*, *Phys. Rev. Lett.* **106** (2011) 171302, [[arXiv:1011.6374](#)].
- [16] J. Zavala, M. Vogelsberger, and M. G. Walker, *Constraining Self-Interacting Dark Matter with the Milky Way’s dwarf spheroidals*, *Mon. Not. Roy. Astron. Soc.* **431** (2013) L20–L24, [[arXiv:1211.6426](#)].
- [17] M. Vogelsberger, J. Zavala, and A. Loeb, *Subhaloes in Self-Interacting Galactic Dark Matter Haloes*, *Mon. Not. Roy. Astron. Soc.* **423** (2012) 3740, [[arXiv:1201.5892](#)].
- [18] T. Bringmann, F. Kahlhoefer, K. Schmidt-Hoberg, and P. Walia, *Strong constraints on self-interacting dark matter with light mediators*, *Phys. Rev. Lett.* **118** (2017), no. 14

- 141802, [[arXiv:1612.00845](#)].
- [19] M. Kaplinghat, S. Tulin, and H.-B. Yu, *Dark Matter Halos as Particle Colliders: Unified Solution to Small-Scale Structure Puzzles from Dwarfs to Clusters*, *Phys. Rev. Lett.* **116** (2016), no. 4 041302, [[arXiv:1508.03339](#)].
- [20] L. G. van den Aarssen, T. Bringmann, and C. Pfrommer, *Is dark matter with long-range interactions a solution to all small-scale problems of Λ CDM cosmology?*, *Phys. Rev. Lett.* **109** (2012) 231301, [[arXiv:1205.5809](#)].
- [21] S. Tulin, H.-B. Yu, and K. M. Zurek, *Beyond Collisionless Dark Matter: Particle Physics Dynamics for Dark Matter Halo Structure*, *Phys. Rev. D* **87** (2013), no. 11 115007, [[arXiv:1302.3898](#)].
- [22] M. Kaplinghat, S. Tulin, and H.-B. Yu, *Direct Detection Portals for Self-interacting Dark Matter*, *Phys. Rev. D* **89** (2014), no. 3 035009, [[arXiv:1310.7945](#)].
- [23] E. Del Nobile, M. Kaplinghat, and H.-B. Yu, *Direct Detection Signatures of Self-Interacting Dark Matter with a Light Mediator*, *JCAP* **10** (2015) 055, [[arXiv:1507.04007](#)].
- [24] C. Kouvaris, I. M. Shoemaker, and K. Tuominen, *Self-Interacting Dark Matter through the Higgs Portal*, *Phys. Rev. D* **91** (2015), no. 4 043519, [[arXiv:1411.3730](#)].
- [25] N. Bernal, X. Chu, C. Garcia-Cely, T. Hambye, and B. Zaldivar, *Production Regimes for Self-Interacting Dark Matter*, *JCAP* **03** (2016) 018, [[arXiv:1510.08063](#)].
- [26] K. Kainulainen, K. Tuominen, and V. Vaskonen, *Self-interacting dark matter and cosmology of a light scalar mediator*, *Phys. Rev. D* **93** (2016), no. 1 015016, [[arXiv:1507.04931](#)]. [Erratum: *Phys.Rev.D* 95, 079901 (2017)].
- [27] T. Hambye and L. Vanderheyden, *Minimal self-interacting dark matter models with light mediator*, *JCAP* **05** (2020) 001, [[arXiv:1912.11708](#)].
- [28] M. Cirelli, P. Panci, K. Petraki, F. Sala, and M. Taoso, *Dark Matter's secret liaisons: phenomenology of a dark $U(1)$ sector with bound states*, *JCAP* **05** (2017) 036, [[arXiv:1612.07295](#)].
- [29] F. Kahlhoefer, K. Schmidt-Hoberg, and S. Wild, *Dark matter self-interactions from a general spin-0 mediator*, *JCAP* **08** (2017) 003, [[arXiv:1704.02149](#)].
- [30] M. Dutta, S. Mahapatra, D. Borah, and N. Sahu, *Self-interacting Inelastic Dark Matter in the light of XENON1T excess*, [arXiv:2101.06472](#).
- [31] D. Borah, M. Dutta, S. Mahapatra, and N. Sahu, *Boosted Self-Interacting Dark Matter and*

- XENON1T Excess*, [arXiv:2107.13176](#).
- [32] L. J. Hall, K. Jedamzik, J. March-Russell, and S. M. West, *Freeze-In Production of FIMP Dark Matter*, *JHEP* **03** (2010) 080, [[arXiv:0911.1120](#)].
- [33] N. Bernal, M. Heikinheimo, T. Tenkanen, K. Tuominen, and V. Vaskonen, *The Dawn of FIMP Dark Matter: A Review of Models and Constraints*, *Int. J. Mod. Phys.* **A32** (2017), no. 27 1730023, [[arXiv:1706.07442](#)].
- [34] R. N. Mohapatra et al., *Theory of neutrinos: A White paper*, *Rept. Prog. Phys.* **70** (2007) 1757–1867, [[hep-ph/0510213](#)].
- [35] P. Minkowski, $\mu \rightarrow e\gamma$ at a Rate of One Out of 10^9 Muon Decays?, *Phys. Lett. B* **67** (1977) 421–428.
- [36] M. Gell-Mann, P. Ramond, and R. Slansky, *Complex Spinors and Unified Theories*, *Conf. Proc. C* **790927** (1979) 315–321, [[arXiv:1306.4669](#)].
- [37] R. N. Mohapatra and G. Senjanovic, *Neutrino Mass and Spontaneous Parity Nonconservation*, *Phys. Rev. Lett.* **44** (1980) 912.
- [38] J. Schechter and J. Valle, *Neutrino Masses in $SU(2) \times U(1)$ Theories*, *Phys. Rev. D* **22** (1980) 2227.
- [39] R. N. Mohapatra and G. Senjanovic, *Neutrino Masses and Mixings in Gauge Models with Spontaneous Parity Violation*, *Phys. Rev. D* **23** (1981) 165.
- [40] G. Lazarides, Q. Shafi, and C. Wetterich, *Proton Lifetime and Fermion Masses in an $SO(10)$ Model*, *Nucl. Phys. B* **181** (1981) 287–300.
- [41] C. Wetterich, *Neutrino Masses and the Scale of $B-L$ Violation*, *Nucl. Phys.* **B187** (1981) 343–375.
- [42] J. Schechter and J. W. F. Valle, *Neutrino Decay and Spontaneous Violation of Lepton Number*, *Phys. Rev.* **D25** (1982) 774.
- [43] R. Foot, H. Lew, X. He, and G. C. Joshi, *Seesaw Neutrino Masses Induced by a Triplet of Leptons*, *Z. Phys. C* **44** (1989) 441.
- [44] A. Falkowski, J. Juknevich, and J. Shelton, *Dark Matter Through the Neutrino Portal*, [arXiv:0908.1790](#).
- [45] V. Gonzalez Macias and J. Wudka, *Effective theories for Dark Matter interactions and the neutrino portal paradigm*, *JHEP* **07** (2015) 161, [[arXiv:1506.03825](#)].
- [46] B. Batell, T. Han, and B. Shams Es Haghi, *Indirect Detection of Neutrino Portal Dark*

- Matter*, *Phys. Rev. D* **97** (2018), no. 9 095020, [[arXiv:1704.08708](#)].
- [47] B. Batell, T. Han, D. McKeen, and B. Shams Es Haghi, *Thermal Dark Matter Through the Dirac Neutrino Portal*, *Phys. Rev. D* **97** (2018), no. 7 075016, [[arXiv:1709.07001](#)].
- [48] P. Bandyopadhyay, E. J. Chun, R. Mandal, and F. S. Queiroz, *Scrutinizing Right-Handed Neutrino Portal Dark Matter With Yukawa Effect*, *Phys. Lett. B* **788** (2019) 530–534, [[arXiv:1807.05122](#)].
- [49] M. Chianese and S. F. King, *The Dark Side of the Littlest Seesaw: freeze-in, the two right-handed neutrino portal and leptogenesis-friendly fimpzillas*, *JCAP* **09** (2018) 027, [[arXiv:1806.10606](#)].
- [50] M. Blennow, E. Fernandez-Martinez, A. Olivares-Del Campo, S. Pascoli, S. Rosauero-Alcaraz, and A. Titov, *Neutrino Portals to Dark Matter*, *Eur. Phys. J. C* **79** (2019), no. 7 555, [[arXiv:1903.00006](#)].
- [51] J. Lamprea, E. Peinado, S. Smolenski, and J. Wudka, *Strongly Interacting Neutrino Portal Dark Matter*, [arXiv:1906.02340](#).
- [52] M. Chianese, B. Fu, and S. F. King, *Minimal Seesaw extension for Neutrino Mass and Mixing, Leptogenesis and Dark Matter: FIMPzillas through the Right-Handed Neutrino Portal*, *JCAP* **03** (2020) 030, [[arXiv:1910.12916](#)].
- [53] P. Bandyopadhyay, E. J. Chun, and R. Mandal, *Feeble neutrino portal dark matter at neutrino detectors*, *JCAP* **08** (2020) 019, [[arXiv:2005.13933](#)].
- [54] A. Berlin and N. Blinov, *Thermal neutrino portal to sub-MeV dark matter*, *Phys. Rev. D* **99** (2019), no. 9 095030, [[arXiv:1807.04282](#)].
- [55] E. Hall, T. Konstandin, R. McGehee, and H. Murayama, *Asymmetric Matters from a Dark First-Order Phase Transition*, [arXiv:1911.12342](#).
- [56] A. Biswas, D. Borah, and D. Nanda, *Light Dirac neutrino portal dark matter with observable ΔN_{eff}* , [arXiv:2103.05648](#).
- [57] S. Tulin, H.-B. Yu, and K. M. Zurek, *Resonant Dark Forces and Small Scale Structure*, *Phys. Rev. Lett.* **110** (2013), no. 11 111301, [[arXiv:1210.0900](#)].
- [58] S. A. Khrapak, A. V. Ivlev, G. E. Morfill, and S. K. Zhdanov, *Scattering in the Attractive Yukawa Potential in the Limit of Strong Interaction*, *Phys. Rev. Lett.* **90** (2003), no. 22 225002.
- [59] A. Kamada, H. J. Kim, and T. Kuwahara, *Maximally self-interacting dark matter: models*

- and predictions, *JHEP* **20** (2020) 202, [[arXiv:2007.15522](#)].
- [60] G. Belanger and J.-C. Park, *Assisted freeze-out*, *JCAP* **1203** (2012) 038, [[arXiv:1112.4491](#)].
- [61] A. Semenov, *LanHEP — A package for automatic generation of Feynman rules from the Lagrangian. Version 3.2*, *Comput. Phys. Commun.* **201** (2016) 167–170, [[arXiv:1412.5016](#)].
- [62] A. Belyaev, N. D. Christensen, and A. Pukhov, *CalcHEP 3.4 for collider physics within and beyond the Standard Model*, *Comput. Phys. Commun.* **184** (2013) 1729–1769, [[arXiv:1207.6082](#)].
- [63] E. Molinaro, C. E. Yaguna, and O. Zapata, *FIMP realization of the scotogenic model*, *JCAP* **1407** (2014) 015, [[arXiv:1405.1259](#)].
- [64] D. Borah and A. Gupta, *New viable region of an inert Higgs doublet dark matter model with scotogenic extension*, *Phys. Rev.* **D96** (2017), no. 11 115012, [[arXiv:1706.05034](#)].
- [65] A. Biswas, D. Borah, and D. Nanda, *When Freeze-out Precedes Freeze-in: Sub-TeV Fermion Triplet Dark Matter with Radiative Neutrino Mass*, *JCAP* **1809** (2018), no. 09 014, [[arXiv:1806.01876](#)].
- [66] D. Borah, M. Dutta, S. Mahapatra, and N. Sahu, *Muon ($g-2$) and XENON1T excess with boosted dark matter in $L\mu - L\tau$ model*, *Phys. Lett. B* **820** (2021) 136577, [[arXiv:2104.05656](#)].
- [67] F. D’Eramo and S. Profumo, *Sub-GeV Dark Matter Shining at Future MeV γ -Ray Telescopes*, *Phys. Rev. Lett.* **121** (2018), no. 7 071101, [[arXiv:1806.04745](#)].
- [68] J. L. Feng, A. Rajaraman, and F. Takayama, *SuperWIMP dark matter signals from the early universe*, *Phys. Rev.* **D68** (2003) 063504, [[hep-ph/0306024](#)].
- [69] D. Borah, D. Nanda, and A. K. Saha, *Common origin of modified chaotic inflation, non thermal dark matter and Dirac neutrino mass*, [arXiv:1904.04840](#).
- [70] D. Borah, B. Karmakar, and D. Nanda, *Common Origin of Dirac Neutrino Mass and Freeze-in Massive Particle Dark Matter*, *JCAP* **1807** (2018), no. 07 039, [[arXiv:1805.11115](#)].
- [71] **CRESST** Collaboration, A. Abdelhameed et al., *First results from the CRESST-III low-mass dark matter program*, *Phys. Rev. D* **100** (2019), no. 10 102002, [[arXiv:1904.00498](#)].

- [72] E. Aprile et al., *Dark Matter Search Results from a One Tonne \times Year Exposure of XENON1T*, [arXiv:1805.12562](#).
- [73] M. Bauer, P. Foldenauer, and J. Jaeckel, *Hunting All the Hidden Photons*, *JHEP* **18** (2020) 094, [[arXiv:1803.05466](#)].
- [74] P. Gondolo and G. Gelmini, *Cosmic abundances of stable particles: Improved analysis*, *Nucl. Phys.* **B360** (1991) 145–179.
- [75] A. Kamada, K. Kaneta, K. Yanagi, and H.-B. Yu, *Self-interacting dark matter and muon $g - 2$ in a gauged $U(1)_{L_\mu - L_\tau}$ model*, *JHEP* **06** (2018) 117, [[arXiv:1805.00651](#)].
- [76] M. Ibe, S. Kobayashi, Y. Nakayama, and S. Shirai, *Cosmological constraint on dark photon from N_{eff}* , *JHEP* **04** (2020) 009, [[arXiv:1912.12152](#)].
- [77] M. Escudero, D. Hooper, G. Krnjaic, and M. Pierre, *Cosmology with A Very Light $L_\mu - L_\tau$ Gauge Boson*, *JHEP* **03** (2019) 071, [[arXiv:1901.02010](#)].
- [78] **CMB-S4** Collaboration, K. N. Abazajian et al., *CMB-S4 Science Book, First Edition*, [arXiv:1610.02743](#).
- [79] **SuperCDMS** Collaboration, R. Agnese et al., *Projected Sensitivity of the SuperCDMS SNOLAB experiment*, *Phys. Rev. D* **95** (2017), no. 8 082002, [[arXiv:1610.00006](#)].
- [80] **DarkSide** Collaboration, P. Agnes et al., *Low-Mass Dark Matter Search with the DarkSide-50 Experiment*, *Phys. Rev. Lett.* **121** (2018), no. 8 081307, [[arXiv:1802.06994](#)].
- [81] **XENON** Collaboration, E. Aprile et al., *Projected WIMP sensitivity of the XENONnT dark matter experiment*, *JCAP* **11** (2020) 031, [[arXiv:2007.08796](#)].
- [82] R. K. Ellis et al., *Physics Briefing Book: Input for the European Strategy for Particle Physics Update 2020*, [arXiv:1910.11775](#).
- [83] C. Cheung, J. T. Ruderman, L.-T. Wang, and I. Yavin, *Kinetic Mixing as the Origin of Light Dark Scales*, *Phys. Rev. D* **80** (2009) 035008, [[arXiv:0902.3246](#)].
- [84] Y. Mambrini, *The ZZ' kinetic mixing in the light of the recent direct and indirect dark matter searches*, *JCAP* **07** (2011) 009, [[arXiv:1104.4799](#)].
- [85] J. D. Clarke, R. Foot, and R. R. Volkas, *Phenomenology of a very light scalar ($100 \text{ MeV} < m_h < 10 \text{ GeV}$) mixing with the SM Higgs*, *JHEP* **02** (2014) 123, [[arXiv:1310.8042](#)].
- [86] E. Ma, *Verifiable radiative seesaw mechanism of neutrino mass and dark matter*, *Phys. Rev.* **D73** (2006) 077301, [[hep-ph/0601225](#)].
- [87] J. A. Casas and A. Ibarra, *Oscillating neutrinos and muon $\rightarrow e$, gamma*, *Nucl. Phys.*

- B618** (2001) 171–204, [[hep-ph/0103065](#)].
- [88] T. Toma and A. Vicente, *Lepton Flavor Violation in the Scotogenic Model*, *JHEP* **01** (2014) 160, [[arXiv:1312.2840](#)].
- [89] A. Ahriche, A. Jueid, and S. Nasri, *Radiative neutrino mass and Majorana dark matter within an inert Higgs doublet model*, *Phys. Rev.* **D97** (2018), no. 9 095012, [[arXiv:1710.03824](#)].
- [90] D. Mahanta and D. Borah, *Fermion Dark Matter with N_2 Leptogenesis in Minimal Scotogenic Model*, [arXiv:1906.03577](#).
- [91] D. Borah, A. Dasgupta, K. Fujikura, S. K. Kang, and D. Mahanta, *Observable Gravitational Waves in Minimal Scotogenic Model*, *JCAP* **08** (2020) 046, [[arXiv:2003.02276](#)].
- [92] K. Griest and D. Seckel, *Three exceptions in the calculation of relic abundances*, *Phys. Rev.* **D43** (1991) 3191–3203.
- [93] **MEG** Collaboration, A. M. Baldini et al., *Search for the lepton flavour violating decay $\mu^+ \rightarrow e^+ \gamma$ with the full dataset of the MEG experiment*, *Eur. Phys. J.* **C76** (2016), no. 8 434, [[arXiv:1605.05081](#)].
- [94] L. Lavoura, *General formulae for $f(1) \rightarrow f(2) \gamma$* , *Eur. Phys. J.* **C29** (2003) 191–195, [[hep-ph/0302221](#)].
- [95] **SINDRUM** Collaboration, U. Bellgardt et al., *Search for the Decay $\mu^+ \rightarrow e^+ e^+ e^-$* , *Nucl. Phys. B* **299** (1988) 1–6.
- [96] A. Baldini et al., *A submission to the 2020 update of the European Strategy for Particle Physics on behalf of the COMET, MEG, Mu2e and Mu3e collaborations*, [arXiv:1812.06540](#).
- [97] **SINDRUM II** Collaboration, C. Dohmen et al., *Test of lepton flavor conservation in $\mu^+ \rightarrow e$ conversion on titanium*, *Phys. Lett. B* **317** (1993) 631–636.
- [98] A. Davidson, *$B - L$ as the fourth color within an $SU(2)_L \times U(1)_R \times U(1)$ model*, *Phys. Rev. D* **20** (1979) 776.
- [99] R. N. Mohapatra and R. E. Marshak, *Local $B-L$ Symmetry of Electroweak Interactions, Majorana Neutrinos and Neutron Oscillations*, *Phys. Rev. Lett.* **44** (1980) 1316–1319. [Erratum: *Phys. Rev. Lett.* **44**, 1643 (1980)].
- [100] R. E. Marshak and R. N. Mohapatra, *Quark - Lepton Symmetry and $B-L$ as the $U(1)$ Generator of the Electroweak Symmetry Group*, *Phys. Lett.* **91B** (1980) 222–224.

- [101] A. Masiero, J. F. Nieves, and T. Yanagida, *B^{-l} Violating Proton Decay and Late Cosmological Baryon Production*, *Phys. Lett.* **116B** (1982) 11–15.
- [102] R. N. Mohapatra and G. Senjanovic, *Spontaneous Breaking of Global B^{-l} Symmetry and Matter - Antimatter Oscillations in Grand Unified Theories*, *Phys. Rev.* **D27** (1983) 254.
- [103] W. Buchmuller, C. Greub, and P. Minkowski, *Neutrino masses, neutral vector bosons and the scale of $B-L$ breaking*, *Phys. Lett.* **B267** (1991) 395–399.
- [104] M. Carena, A. Daleo, B. A. Dobrescu, and T. M. P. Tait, *Z' gauge bosons at the Tevatron*, *Phys. Rev.* **D70** (2004) 093009, [[hep-ph/0408098](#)].
- [105] G. Cacciapaglia, C. Csaki, G. Marandella, and A. Strumia, *The Minimal Set of Electroweak Precision Parameters*, *Phys. Rev. D* **74** (2006) 033011, [[hep-ph/0604111](#)].
- [106] **ATLAS** Collaboration, M. Aaboud et al., *Search for new high-mass phenomena in the dilepton final state using 36.1 fb^{-1} of proton-proton collision data at $\sqrt{s} = 13 \text{ TeV}$ with the ATLAS detector*, [arXiv:1707.02424](#).
- [107] **ATLAS** Collaboration, G. Aad et al., *Search for high-mass dilepton resonances using 139 fb^{-1} of pp collision data collected at $\sqrt{s} = 13 \text{ TeV}$ with the ATLAS detector*, *Phys. Lett.* **B796** (2019) 68–87, [[arXiv:1903.06248](#)].
- [108] **CMS** Collaboration, A. M. Sirunyan et al., *Search for high-mass resonances in dilepton final states in proton-proton collisions at $\sqrt{s} = 13 \text{ TeV}$* , *JHEP* **06** (2018) 120, [[arXiv:1803.06292](#)].